

Article

The Impact of Functionality and Porous System of Nanostructured Carriers Based on Metal–Organic Frameworks of UiO-66-Type on Catalytic Performance of Embedded Au Nanoparticles in Hydroamination Reaction

Vera I. Isaeva ^{1,*}, Vladimir V. Chernyshev ^{2,3}, Vadim V. Vergun ¹, Danil A. Arkhipov ¹, Grigory S. Deyko ¹, Lev M. Glukhov ¹, Gennady I. Kapustin ¹, Olga P. Tkachenko ¹ and Leonid M. Kustov ^{1,2}

¹ N.D. Zelinsky Institute of Organic Chemistry, Russian Academy of Sciences, 47 Leninsky Prospect, 119991 Moscow, Russia

² Department of Chemistry, M.V. Lomonosov Moscow State University, 1-3 Leninskie Gory, 119991 Moscow, Russia

³ A.N. Frumkin Institute of Physical Chemistry and Electrochemistry, Russian Academy of Sciences, Building 4, 31 Leninsky Prospect, 119071 Moscow, Russia

* Correspondence: sharf@ioc.ac.ru



Citation: Isaeva, V.I.; Chernyshev, V.V.; Vergun, V.V.; Arkhipov, D.A.; Deyko, G.S.; Glukhov, L.M.; Kapustin, G.I.; Tkachenko, O.P.; Kustov, L.M. The Impact of Functionality and Porous System of Nanostructured Carriers Based on Metal–Organic Frameworks of UiO-66-Type on Catalytic Performance of Embedded Au Nanoparticles in Hydroamination Reaction. *Catalysts* **2023**, *13*, 133. <https://doi.org/10.3390/catal13010133>

Academic Editors: Leonarda Liotta, Salvatore Scirè and Ivan V. Kozhevnikov

Received: 28 November 2022

Revised: 24 December 2022

Accepted: 4 January 2023

Published: 6 January 2023



Copyright: © 2023 by the authors. Licensee MDPI, Basel, Switzerland. This article is an open access article distributed under the terms and conditions of the Creative Commons Attribution (CC BY) license (<https://creativecommons.org/licenses/by/4.0/>).

Abstract: New methods for the preparation of metal–organic frameworks UiO-66 and NH₂-UiO-66 with a hierarchical porous structure were developed using the MW-assisted technique under atmospheric pressure. The synthesized nanostructured meso-UiO-66 and meso-NH₂-UiO-66 matrices were utilized as Au nanoparticle carriers. The resulting Au@meso-UiO-66 and Au@NH₂-UiO-66 nanohybrids were studied in the reaction of phenylacetylene hydroamination with aniline into imine ([phenyl-(1-phenylethylidene)amine]) for the first time. Their catalytic behavior is significantly determined by a combination of factors, such as a small crystal size, micro–mesoporous structure, and functionality of the UiO-66 and NH₂-UiO-66 carriers, as well as a high dispersion of embedded gold nanoparticles. The Au@meso-UiO-66 and Au@NH₂-UiO-66 nanocatalysts demonstrate high activities (TOF), with conversion and selectivity values over 90. This excellent catalytic performance is comparable or even better than that demonstrated by heterogeneous systems based on conventional inorganic and inorganic supports known from the literature.

Keywords: MW-assisted technique; metal–organic frameworks UiO-66 and NH₂-UiO-66; gold nanoparticles; catalysis; hydroamination

1. Introduction

N-containing molecules are present in natural and synthetic products such as nucleic acids, alkaloids, colorants, agrochemicals and pharmaceuticals [1]. Among other organic transformations, hydroamination of alkynes allows the direct formation of C–N bonds through the addition of amines to unsaturated C–C bonds [2–4] and thereby provides atom-economical access to highly valuable organic molecules. In this way, alkynes are converted into reactive species (enamines, imines) that can be used as intermediates in subsequent transformations, which are involved in industrially important processes.

From a thermodynamical point of view, the direct addition of amines to alkenes is feasible [5]. In general, a high activation barrier exists for the direct addition of amines across C–C multiple bonds, which arise from electrostatic repulsion between the electron lone pair at the nitrogen atom and the electron-rich π -bond of the alkene or alkyne. Therefore, hydroamination requires catalyst utilization, such as acids including zeolites [6], bases, metal complexes [7] and supported metal nanoparticles [8,9].

Among other heterogeneous systems, Au-based catalysts have attracted much attention over the last few years [10–12]. The use of solid supports for the immobilization of

gold nanoparticles (Au-NP) allows the controlled incorporation of catalytic active sites, thereby contributing to the improvement of Au-NP catalytic performance [13,14].

Various materials, such as polymers, carbons and inorganic oxides, were employed as supports in order to prevent the agglomeration of the gold nanoparticles [15,16]. Among the various carriers for the gold active phase, metal–organic frameworks provide a number of benefits [17]. Metal–organic frameworks (MOFs) are nanoporous crystalline materials, which were considered promising functional materials as regards their applications for gas storage and separation [18–20], catalysis [21], energy storage [22] and drug delivery [23–27]. In MOF networks, the lattice contains metal ions or metal clusters held by rigid, more often, aromatic bi- or multi-podal organic linkers [28]. A large diversity of MOFs based on virtually any transition metal, as well as alkaline earth and rare earth metals, were reported. In addition to the rich composition diversity, one of the important features that make MOFs so appropriate in heterogeneous catalysis is their high porosity, large surface area and tunable chemical properties [29].

During the last few decades, MOFs have been utilized as a new type of support for noble metal nanoparticles [30]. Because of the well-ordered pore structure with rich functionality and diverse microenvironments, MOF host matrices contribute to the high and homogeneous dispersion of metal nanoparticles (M-NP), and further modulate their catalytic properties. The combination of the solid porous structure of MOFs and the high catalytic activities of metal nanoparticles offers advantages over other catalysts, such as shorter reaction times and excellent recyclability. In particular, embedding the Au-NP in the MOF host matrices may improve their catalytic performances [31].

Among various MOF matrices explored for Au-NP immobilization, the UiO-66 ($Zr_6O_4(OH)_4(bdc)_6$, bdc = benzene-1,4-dicarboxylate) material and associated Zr-based structures, such as NH_2 -UiO-66, UiO-67 and UiO-68 are of particular interest, due to the high thermal and chemical stability under a wide range of conditions [32,33]. The UiO-66(Zr) framework is based on bdc linkers and its amino-functionalized counterpart NH_2 -UiO-66 is composed of 2-aminobenzene-1,4-dicarboxylate (abdc) linkers.

Due to Zr^{4+} Lewis acid sites and Zr-OH Brønsted acid sites, the UiO-66(Zr) and NH_2 -UiO-66 matrices are highly active, stable and reusable heterogeneous systems for acid catalysis [34]. Additionally, NH_2 -linkers in the NH_2 -UiO-66 structure may serve as Brønsted base centers.

It is known that in the UiO-66 framework, structure defects or missing bdc linkers create accessible Zr^{4+} sites [35]. In particular, the catalytic activity and selectivity of UiO-66 could be effectively modulated through the generation of Zr defective sites in the structure of the UiO-66(Zr) matrix. These defects are coordinatively unsaturated Zr^{4+} ions with Lewis acid properties. Therefore, the catalytic activity increases along with the number of missing linkers [36].

A number of experimental techniques are developed to control the amount of open Zr sites within the UiO-66 material [37,38]. Moreover, these defects result in the formation of the mesopore structures in the UiO-66(Zr) and NH_2 -UiO-66 matrices that assist the mass transport of bulky molecules of the reactants, intermediates and reaction products during catalytic reactions associated with fine chemical synthesis over Au catalysts.

Despite attractive characteristics of UiO-66(Zr)-type materials as carriers, the examples of gold-containing catalysts supported on UiO-66(Zr) and NH_2 -UiO-66 carriers are rather scarce. An example is the preparation of Au@ NH_2 -UiO-66 nanohybrids and their utilization as selective catalysts for tandem catalytic reactions, i.e., the selective oxidation of primary alcohols in tandem with Knoevenagel condensation reactions [39]. In [2], Au-Pd alloy-based catalysts were prepared using an NH_2 -UiO-66 matrix as support and utilized as catalysts in the reductive amination of aldehydes with nitroarenes.

Noteworthy, the direct hydroamination of alkynes over gold-containing catalysts based on MOF carriers remains almost unexplored. To the best of our knowledge, there are only limited examples of performing the hydroamination reaction over metal nanoparticles supported on MOF carriers. For instance, the hydroamination of alkynes with substituted

anilines was carried out over a Pd@NiBDP hybrid catalyst, which was a metal–organic framework with Ni²⁺ ions and pyrazolate linkers modified by post-synthesis strategy with Pd²⁺ complexes [Pd(NH₃)₄]²⁺ [40]. Recently, we reported the catalytic hydroamination of phenylacetylene with aniline in an air atmosphere over Au-NP embedded in the mesoporous metal–organic frameworks NH₂-MIL-101(Al) and MIL-100(Fe) [41], microporous boron imidazolate framework BIF-67 and zeolite imidazolate framework ZIF-67 [42]. The role of the composition and textural properties of MOF carriers were studied. For instance, the Fe³⁺ ions in the MIL-100(Fe) framework are open Lewis acid sites. It was suggested that these inorganic nodes in the framework impacted the activity of the catalytic system in hydroamination.

In this study, hierarchically micro–mesostructured meso-UiO-66 and meso-NH₂-UiO-66 materials composed of extremely small nanocrystallites were synthesized using the MW-assisted technique following the original procedures. The highly dispersed Au-NPs were embedded in the nanosized meso-UiO-66 and meso-NH₂-UiO-66 host matrices via the impregnation method. The catalytic performance of the produced Au@meso-UiO-66 and Au@NH₂-UiO-66 nanohybrids was studied in the model reaction of phenylacetylene with aniline under an air atmosphere.

A special goal of this work was an investigation of the different factors, which may play a role in the control of activity and stability of supported Au-NPs during catalytic reactions. In particular, it was shown how the judicious choice of the MOF host matrix structure, dispersion and composition, in particular, the intrinsic Lewis and Brønsted acid sites, as well as the appropriate preparation procedure of the gold nanohybrids, may enhance the gold catalytic properties in the hydroamination reaction.

2. Results

2.1. Synthesis of the meso-UiO-66, meso-NH₂-UiO-66 Matrices, and Au@meso-UiO-66 and Au@meso-NH₂-UiO-66 Nanohybrids

The hierarchically structured matrices of meso-UiO-66 and meso-NH₂-UiO-66 were synthesized according to original procedures using the MW-activation technique under atmospheric pressure. It was established that the mesopore fraction is determined by the solvent nature, Zr⁴⁺ ion source and reagent ratio in the preparation course. In particular, according to original procedures, the meso-UiO-66 and meso-NH₂-UiO-66 samples were prepared using ZrOCl₂·8H₂O as Zr⁴⁺ ion sources instead of the hazardous ZrCl₄ reagent utilized in a number of relevant works [43].

The Au@meso-UiO-66 and Au@meso-NH₂-UiO-66 nanohybrids were prepared using the impregnation method according to [31]. The Au content in the synthesized nanomaterials is listed in Table S1. After examinations of the nanocatalysts in the hydroamination reaction, only negligible decreases in the gold content took place. This observation indicates the preferential location of Au-NPs in the pores of the meso-UiO-66 and meso-NH₂-UiO-66 carriers, which prevents gold leaching in the catalysis course.

2.2. The Studies of the Pore Systems of the meso-UiO-66, meso-NH₂-UiO-66, and Au@meso-UiO-66 and Au@meso-NH₂-UiO-66 Materials

The N₂-low temperature adsorption isotherms of the microporous (micro-UiO-66) reference sample synthesized by the classical solvothermal procedure [32], meso-UiO-66 and meso-NH₂-UiO-66 materials, are shown in Figure 1. The micro-UiO-66 material demonstrates a classical type I isotherm, which is characteristic of microporous materials, while the adsorption isotherm measured for the meso-UiO-66 matrix belonged to the IV type, which is characteristic of the mesoporous materials. The meso-NH₂-UiO-66 material shows an adsorption isotherm, which is rather intermediate between type II and is characteristic for the adsorbents featuring a wide range of pore sizes and for type IV.

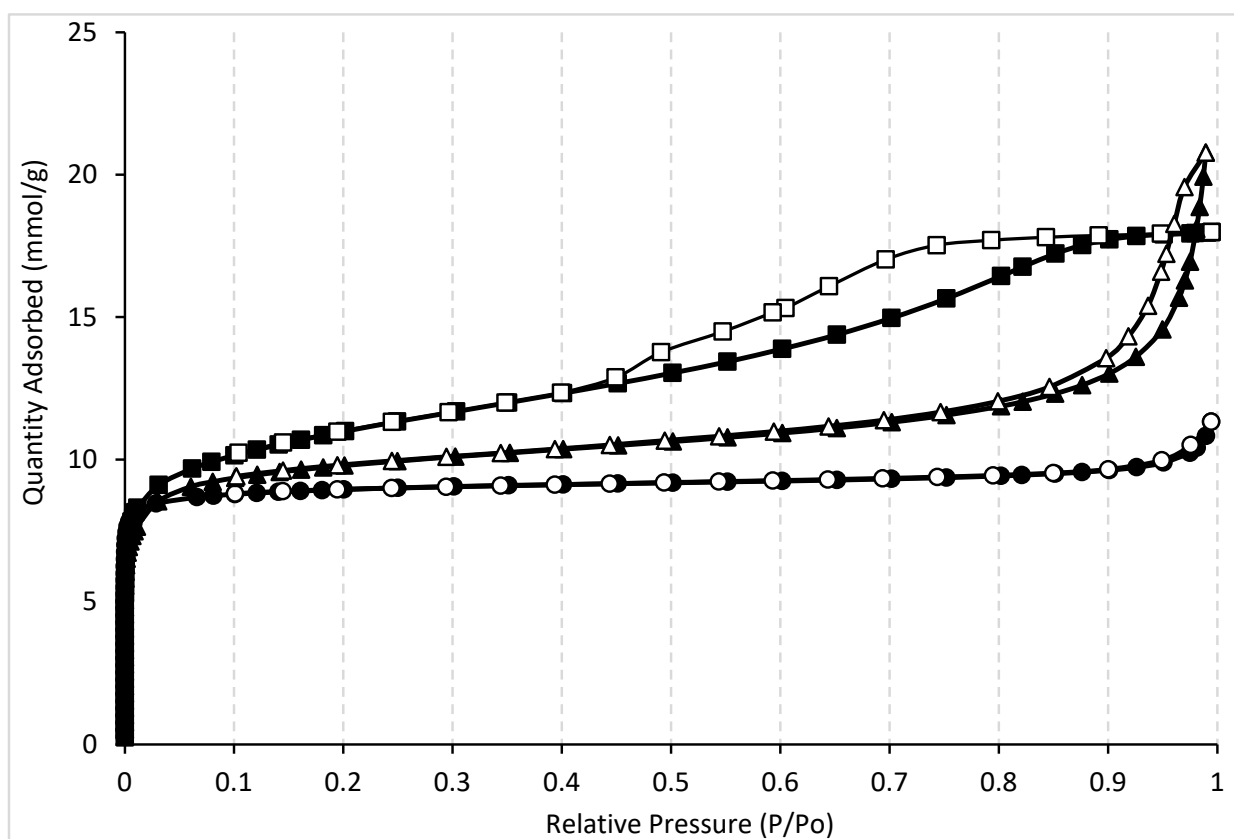


Figure 1. N_2 -adsorption–desorption isotherms measured at 77 K. for the micro-UiO-66 (●), meso-UiO-66 (■) and meso-NH₂-UiO-66 (▲) materials (solid symbols—adsorption, open symbols—desorption) and Au@meso-NH₂-UiO-66-before- and -after-catalysis nano hybrids.

The Au@meso-UiO-66-before- and -after-catalysis and Au@meso-NH₂-UiO-66-before- and -after-catalysis nano hybrids show the N_2 -low temperature adsorption isotherms belonging to the type IV (Figure 2) that indicate their mesoporous structure. Interestingly to note, after Au-NP deposition, the character of the isotherm measured for the meso-NH₂-UiO-66 matrix undergoes some changes and it became a real type IV isotherm for the Au@meso-NH₂-UiO-66-before- and -after-catalysis systems.

All isotherms measured for the meso-NH₂-UiO-66 and meso-NH₂-UiO-66 carriers (Figure 1), as well as the Au-containing nano hybrids based on them (Figure 2), show hysteresis loops that indicate the mesopore contents in these materials. In particular, the hysteresis loop on the isotherm measured for the Au@meso-NH₂-UiO-66-before-catalysis nanomaterial is more pronounced when compared to the pristine meso-NH₂-UiO-66 carrier, which corresponds to a more significant mesopore fraction in this sample.

The N_2 -low temperature adsorption isotherms measured for the Au@meso-UiO-66-before- and -after-catalysis nano hybrids are rather similar to the isotherm for the meso-UiO-66 porous host. However, the hysteresis loops on the isotherms of the gold-containing nanomaterials are also larger when compared to the isotherm of the pristine carrier.

The textural characteristics of the meso-UiO-66 and meso-NH₂-UiO-66 matrices, as well as the Au@meso-UiO-66 and Au@meso-NH₂-UiO-66 nano hybrids-before- and -after-catalysis tested in the hydroamination reaction, are shown in Table 1.

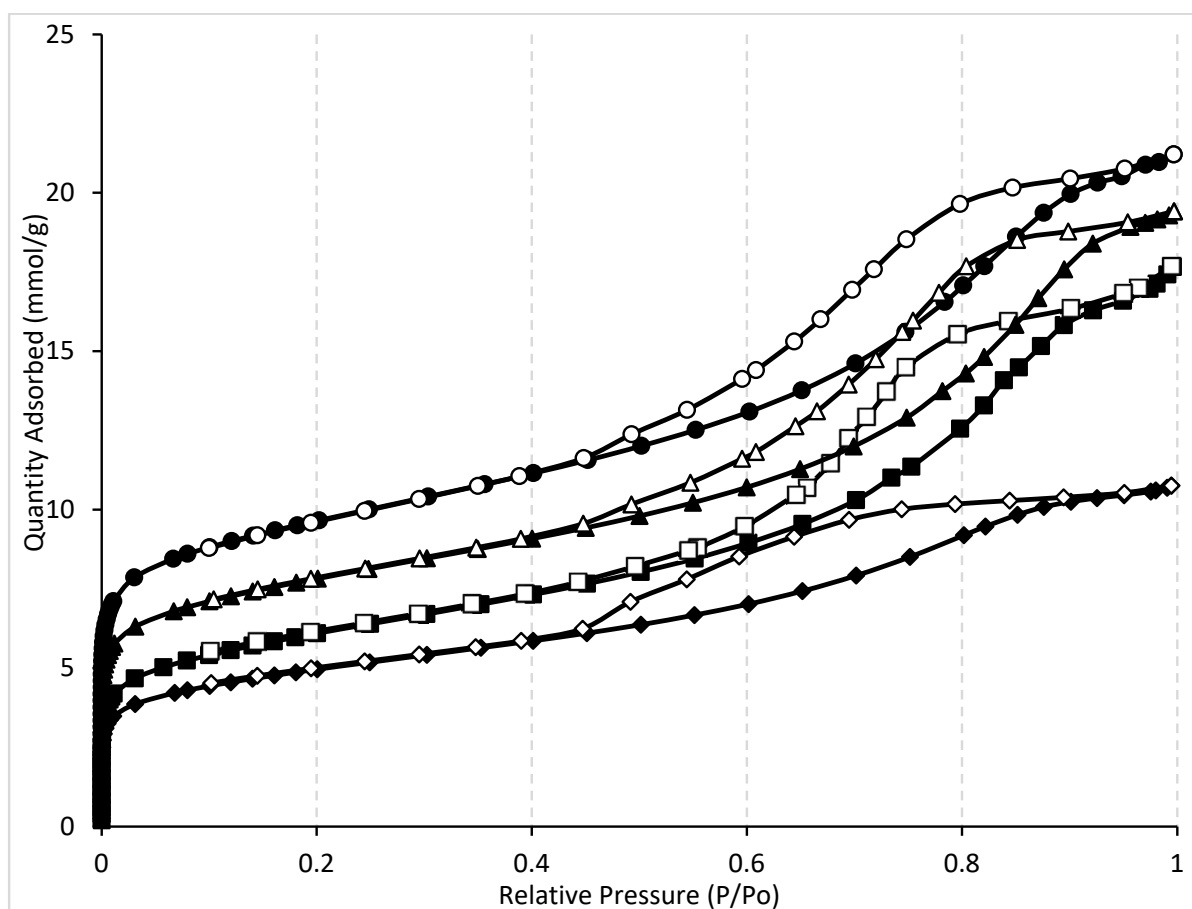


Figure 2. N₂-adsorption–desorption isotherms measured at 77 K. for the catalysts Au@meso-UiO-66-before- (●) and -after-(▲) catalysis nanohybrids; Au@meso-NH₂-UiO-66-before- (■) and -after-catalysis nanohybrids (◆). (solid symbols—adsorption, open symbols—desorption).

Table 1. Textural characteristics for the meso-UiO-66 and meso-NH₂-UiO-66 matrices as well as Au@meso-UiO-66 and Au@meso-NH₂-UiO-66 nanohybrids (Au-NP content is ~5 wt.%) before and after catalysis. The specific surface area was calculated according to ISO 9277-2010.

Material	A _{BET} (ISO) m ² /g	A _{meso} m ² /g	V _{tot.} ^a cm ³ /g	V _{micro} ^b cm ³ /g	V _{meso} ^c cm ³ /g	Pore Width, nm
UiO-66	807	34	0.393	0.287	0.096	0.6–2.0
meso-UiO-66	904	345	0.624	0.243	0.381	0.6–2.0; 2–15
5%Au@meso-UiO-66 before catalysis	786	404	0.735	0.183	0.552	0.6–2.0; 2–20
5%Au@meso-UiO-66 after catalysis	633	353	0.673	0.126	0.547	0.6–2.0; 2–20
meso-NH ₂ -UiO-66	849	129	0.720	0.285	0.435	0.6–2.0; 2–50
5%Au@meso-NH ₂ -UiO-66 before catalysis	489	328	0.613	0.078	0.535	0.6–2.0; 2–30
5%Au@meso-NH ₂ -UiO-66 after catalysis	399	255	0.373	0.070	0.303	0.6–2.0; 2–20

^a from adsorption value at $p/p_0 = 0.99$; ^b The micropore volume was calculated by “t-plot” method. ^c cumulative mesopore volume calculated by desorption branch by BJH method and adsorption film thickness according to Harkins and Jura method reported in [44].

The values of the specific surface and total pore volume measured for the meso-UiO-66 and meso-NH₂-UiO-66 samples (Table 1) are a bit higher than those measured for the micro-UiO-66 material. The latter has textural characteristics, which are almost identical to

the characteristics reported elsewhere [32]. The meso-UiO-66 sample has a mesopore area around an order higher than its microporous counterpart (Table 1). Furthermore, its specific surface area is higher than that measured for the meso-NH₂-UiO-66 material, while the latter has the highest pore volume when compared to other studied systems. Therefore, both the meso-UiO-66 and meso-NH₂-UiO-66 samples are hierarchically meso/micro-structured materials, in which the mesopore content is significantly higher than the micropore one.

The meso-UiO-66 material shows a micropore size distribution with two maxima around 0.65 nm and 0.8 nm (Figure S1a), while its amino-functionalized counterpart has a more substantial content of small micropores and narrow micropore size distribution with a maximum around 0.6 nm (Figure S1b). However, both materials have similar micropore widths of ~0.6–2.0 nm (Table 1).

The meso-UiO-66 material features a mesopore size distribution in a narrower range with two maxima around 4 and 6 nm (Figure S2a) than the meso-NH₂-UiO-66 matrix with a mesopore size distribution changing in a broad range of 3–60 nm without a remarkable maximum (Figure S2b). Therefore, the mesopore width for the meso-UiO-66 sample differs in the range of 2–15, while the mesopore width for the meso-NH₂-UiO-66 material changes in the range of 2–50 nm.

These data can explain discrepancies in mesopore fraction values determined for both materials. The meso-UiO-66 material has a more significant mesopore fraction expressed as mesopore area (A) than its meso-NH₂-UiO-66 counterpart. Obviously, the adsorption isotherm measured for the meso-UiO-66 material has a more pronounced hysteresis loop than that measured for the meso-NH₂-UiO-66 matrix (Figure 1). Vice versa, the latter has a higher mesopore volume than its analog without amino groups in organic linkers.

It can be suggested while analyzing the experimental results on low-temperature N₂ adsorption that the difference in the porous structures of the meso-UiO-66 and meso-NH₂-UiO-66 matrices may contribute to the specific location and confinement for embedded gold nanoparticles.

The specific surface areas (BET) of the meso-UiO-66 and meso-NH₂-UiO-66 matrices are decreased after Au-NP embedding (Table 1). This specific area drop is much more pronounced (around twice) for the Au@meso-NH₂-UiO-66-before-catalysis nanohybrid.

The micropore volume in the Au@meso-UiO-66-before-catalysis nanohybrid is a bit reduced when compared to the pristine porous matrix. A further decrease in the micropore volume is observed for the Au@meso-UiO-66-after-catalysis nanomaterial. However, this micropore volume drop is not so significant when compared with the Au@meso-NH₂-UiO-66-before- and -after-catalysis nanohybrids. The latter show a dramatic decrease in micropore volume until almost the same values (Table 1, Figure S1) when compared with the pristine meso-NH₂-UiO-66 material.

The mesopore content expressed in the mesopore area and mesopore volume is increased after Au-NP deposition for both Au@meso-UiO-66-before-catalysis and Au@meso-NH₂-UiO-66-before-catalysis nanomaterials (Table 1). In particular, the mesopore fraction expressed in the mesopore area is slightly decreased for the Au@meso-UiO-66-before-catalysis to the value obtained for the pristine meso-UiO-66 carrier, while the mesopore volume values remain almost the same for both Au@meso-UiO-66-before- and -after-catalysis nanohybrids.

Unlike the Au@meso-UiO-66-after-catalysis system, the mesopore volume in the Au@meso-NH₂-UiO-66-after-catalysis nanomaterial is significantly decreased when compared to those of the meso-NH₂-UiO-66 matrix and Au@meso-NH₂-UiO-66-before-catalysis nanomaterial. However, the mesopore surface in the Au@meso-NH₂-UiO-66-after-catalysis nanohybrid is higher when compared with the pristine carrier, but yet lower than that measured for the Au@meso-NH₂-UiO-66-before-catalysis system.

The mesopore width (Table 1, Figure S3a,) for the Au@meso-UiO-66-before- and -after-catalysis nanohybrids differs in a slightly broader range (2–20 nm) than that in the pristine meso-UiO-66 matrix (2–15 nm). Vice versa, the mesopore width differs in the narrower range (2–30 nm) for the Au@meso-NH₂-UiO-66-before-catalysis and an even narrower

range for the Au@meso-NH₂-UiO-66-after-catalysis nanohybrid (2–20 nm) when compared with the pristine carrier (Table 1, Figure S3b).

2.3. Au-NP Dispersion in the Au@meso-UiO-66 and Au@meso-NH₂-UiO-66 Nanohybrids

The TEM micrographs (Figure 3) show that both pristine meso-UiO-66 and meso-NH₂-UiO-66 materials are composed of very small crystallites with average sizes of ~8 nm and ~14 nm, respectively. These nanoparticles are combined in agglomerates with sizes of ~200 nm for the meso-UiO-66 sample and ~50–100 nm for the meso-NH₂-UiO-66 system.

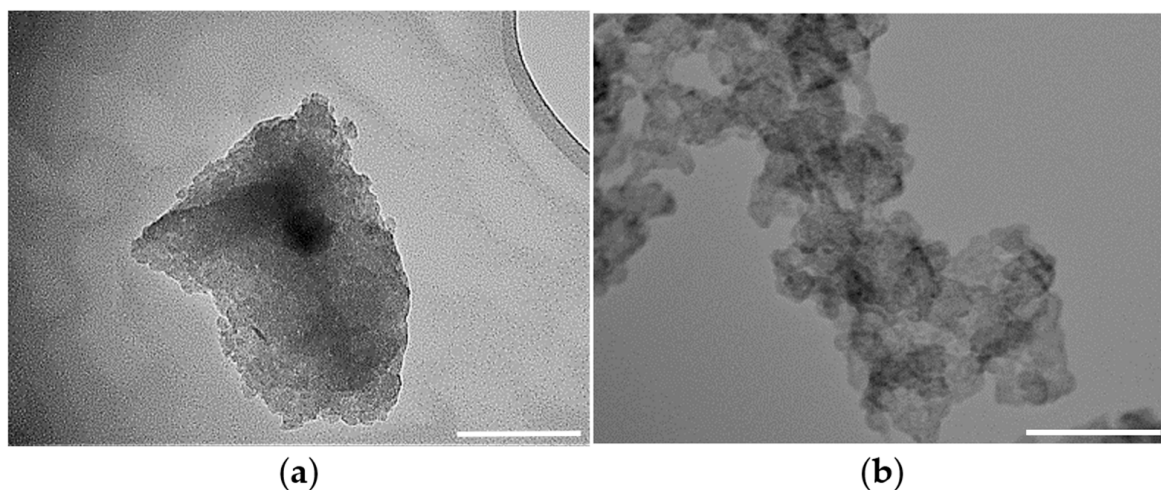


Figure 3. TEM micrographs of the pristine (a) meso-UiO-66 (scale bar is 200 nm) and (b) meso-NH₂-UiO-66 (scale bar is 50 nm) materials.

The TEM results justify the formation of well-dispersed small Au-NP in both the meso-UiO-66 and meso-NH₂-UiO-66 matrices. It can be seen that there are rather small Au-NP with similar calculated average sizes, i.e., around 7.3 nm in the meso-UiO-66 nanomaterial (Figures 4 and S3) and ~7.7 nm in the meso-NH₂-UiO-66 (Figures 5a and S4) nanohybrid. These Au-NP are located mainly inside the host matrices.

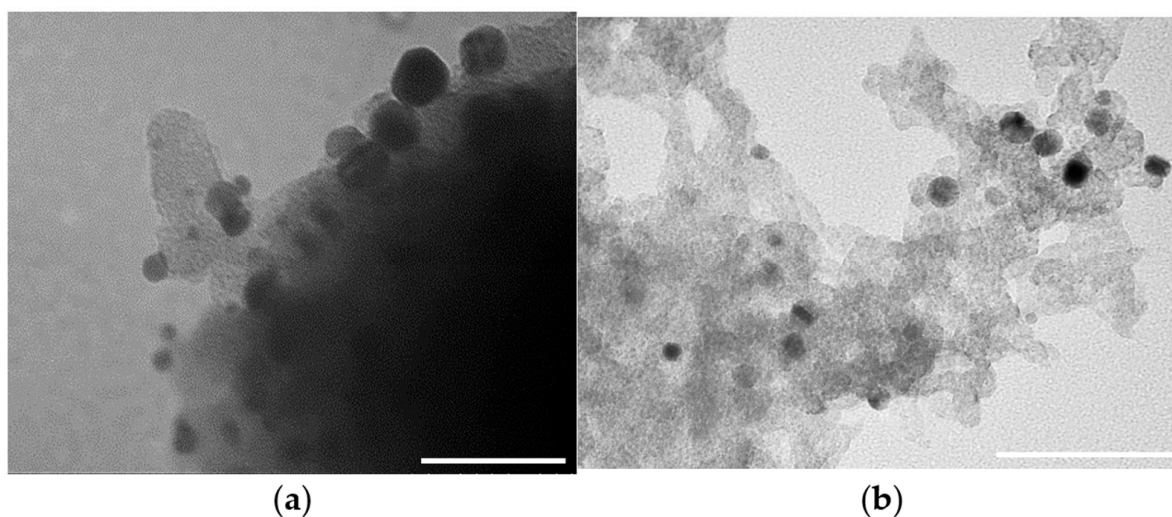


Figure 4. TEM micrographs of the (a) Au@meso-UiO-66-before-catalysis (scale bar is 100 nm) and (b) Au@meso-UiO-66-after-catalysis (scale bar is 50 nm) nanohybrids.

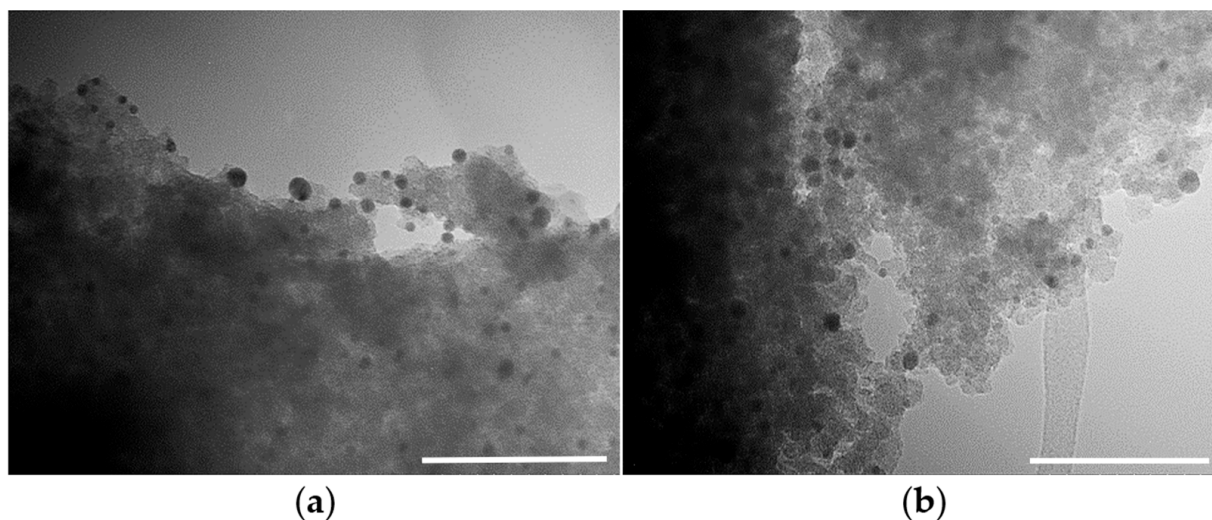


Figure 5. TEM micrographs of the (a) Au@meso-NH₂-UiO-66-before-catalysis (scale bar is 100 nm) and (b) Au@meso-NH₂-UiO-66-after-catalysis (scale bar is 200 nm) nano hybrids.

It is interesting to note that an almost similar gold particle size was observed for the Au@ZIF-67 nano hybrids based on the zeolitic imidazolate framework ZIF-67 [35].

A high dispersion (Figure 4b) in the Au@meso-UiO-66-after-catalysis nano hybrid remains after one cycle of catalysis. The comparison of TEM micrographs for the Au@meso-UiO-66-before-catalysis (Figure 4a) and Au@meso-UiO-66-before-catalysis (Figure 4b) nano hybrids reveals that in the first case, there are more relatively large gold nanoparticles (with average sizes 14–16 nm, Figure S4) on the catalyst surface. The slight decrease in the average Au-NP size (around 6.8 nm, Figure S5) when compared with that for the Au@meso-UiO-66-before-catalysis nano hybrid could be explained by negligible leaching (Table S1) of the gold nanoparticles located on the catalyst surface.

A careful inspection of the TEM micrograph (Figure 5b) of the Au@meso-NH₂-UiO-66-after-catalysis system indicates a slight aggregation of Au-NP embedded in the meso-NH₂-UiO-66 matrix. In this case, there are two fractions of the gold nanoparticles. The first of them (as the main component) is composed of Au-NP with calculated average sizes of ~6–7 nm, while the second one (as a minor component) is constituted of Au-NP with an average size of ~15 nm (Figure S6) located on the carrier surface or near-surface layers. This phenomenon could be assigned to the particular mobility of the deposited Au-NP [45].

2.4. Structural Examinations

The Rietveld refinement (performed with the MRUA program [46]) of the diffraction pattern of the as-synthesized sample meso-UiO-66 with fixed atomic coordinates taken from the known crystal structure [32] (CCDC refcode RUBTAK) demonstrates (Figure 6) that the sample has the classical cubic (Fm-3m) structure of UiO-66. The cubic unit cell parameter was refined to 20.705(2) Å.

The powder pattern of the meso-NH₂-UiO-66 sample (Figure 7) is almost the same as in the case of the meso-UiO-66 material (Figure 8).

The powder patterns of the Au@meso-UiO-66 and Au@meso-NH₂-UiO-66 nano hybrids display the crystallinity of the obtained materials (Figures 8 and 9, red curves). Embedded Au-NPs do not change the cubic structural motif of the pristine materials UiO-66 and NH₂-UiO-66. The positions of all diffraction peaks of Au@meso-UiO-66 and Au@meso-NH₂-UiO-66 nano hybrids are consistent with those for the pristine UiO-66 matrix. The crystallinity of the Au@UiO-66 nano hybrids remains intact after the hydroamination reaction using these catalytic systems (Figures 8 and 9, blue curves). No significant changes in the peak intensities are observed in the powder diffraction patterns of the Au@UiO-66 nano hybrids after three catalytic cycles.

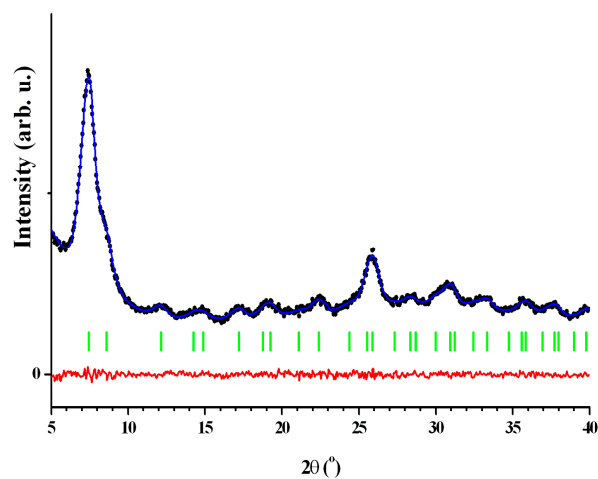


Figure 6. The Rietveld plot for the meso-UiO-66 material showing the experimental (black dots), calculated (blue) and difference (red) curves. The vertical green bars denote calculated positions of the peaks for the cubic crystal structure UiO-66.

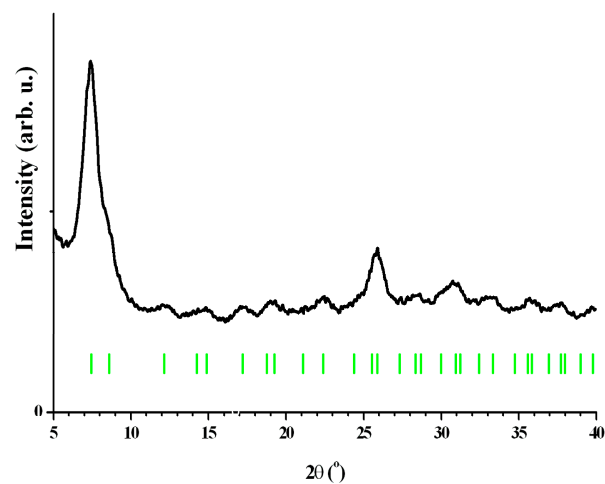


Figure 7. XRD powder pattern of the meso-NH₂-UiO-66 sample. The vertical bars denote calculated positions of the peaks for the cubic crystal structure UiO-66.

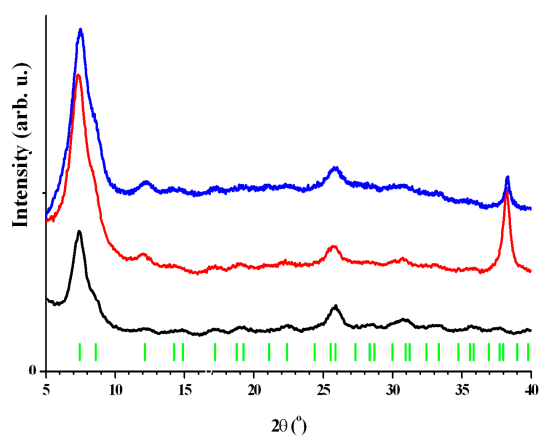


Figure 8. XRD patterns of the meso-UiO-66 (black), Au@meso-UiO-66-before-catalysis (red) and Au@meso-UiO-66-after-catalysis (blue) samples. The vertical bars denote calculated positions of the peaks for the cubic crystal structure UiO-66.

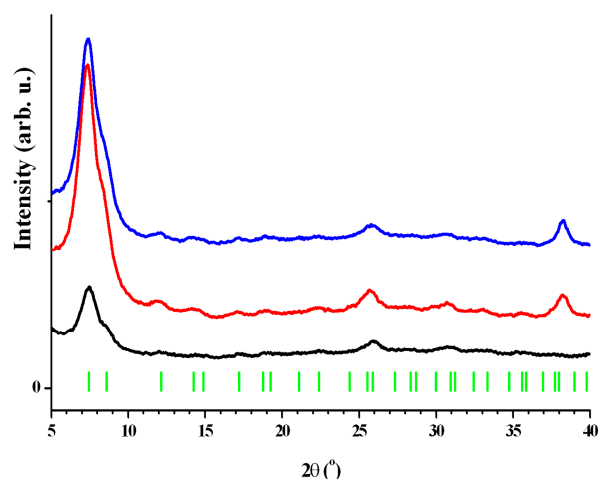


Figure 9. XRD patterns of the meso-NH₂-UiO-66 (black), 5%Au@meso-NH₂-UiO-66-before-catalysis (red) and Au@meso-NH₂-UiO-66-after-catalysis (blue) samples. The vertical bars denote calculated positions of the peaks for the cubic crystal structure UiO-66.

The only observed feature concerns the decrease in the peak from gold at an angle of 38.2° corresponding to reflection from the (111) plane in the cubic Fm-3m structure of Au in the powder pattern of Au@meso-UiO-66-after-catalysis when compared with that in Au@meso-UiO-66-before-catalysis (Figure 8).

The Au peaks at 38.2° in the powder patterns of Au@meso-NH₂-UiO-66-before-catalysis and Au@meso-NH₂-UiO-66-after-catalysis have no differences in height (Figure 9). Note that the Au@meso-NH₂-UiO-66-after-catalysis nanohybrid was studied by XRD after one catalytic cycle, while the Au@meso-UiO-66-after-catalysis was analyzed after.

Additionally, the amino groups in the meso-NH₂-UiO-66 material could coordinate with Au-NP and prevent them, to some extent, from leaching and sintering during the hydroamination reaction. This stabilizing effect of amino groups for M-NP in the MOF matrices was reported elsewhere [47].

2.5. DRIFTS Investigations of the Synthesized UiO-66 Type Materials

Figure S7 shows the IR spectra of both meso-UiO-66 samples before (as received) and after treatment in a vacuum at 150 °C at full scale. There are two differences between the two spectra. There is a small peak at about 5200 cm⁻¹ belonging to the presence of adsorbed water in the spectrum of the as-received sample. In the same spectrum, there is a wide region between 3500 and 3200 cm⁻¹ that is characteristic of the interaction of the surface with adsorbed water and other molecules. Vacuum treatment at 150 °C leads to the removal of all residuary substances.

Figures S8–S10 show the IR spectra of the meso-UiO-66 sample after evacuation in the regions of 3800–3400, 3400–2200 and 2200–1000 cm⁻¹, correspondingly. The small intensive band at 3689 cm⁻¹ belongs to the stretching vibration of O-H groups in the bridge (Zr⁴⁺)₂-OH [48,49] or/and μ₃-OH fragments [50]. The intensive band at 3671 cm⁻¹ and the small band at 3653 cm⁻¹ are characteristic of O-H groups in the bridge μ₃-OH [51,52] (Figure S8). The bands at 3075, 2986, 2947 and 2884 cm⁻¹ (Figure S9) characterize asymmetrical and symmetrical stretching vibrations in -CH₃ and -CH₂ fragments of organic linkers. There are a few bands in the region of 1953–1670 cm⁻¹ that belong to overtones of the deformation vibration δC-H bond (nonlinear and multiple) (Figure S10). In the same place, there are the bands of the stretching vibration νC-C in aromatic rings in the 1650–1550 cm⁻¹ region. The bands at 1568 and 1460 cm⁻¹ νC=C are in the aromatic ring. The bands in the 1300–1000 cm⁻¹ region belong to the plain deformation vibration of the aromatic ring.

Figure S11 shows the IR spectra of both the meso-NH₂-UiO-66 samples before (as-received) and after treatment in a vacuum at 150 °C at full scale. There are two differences between the two spectra. There is a small peak at about 5200 cm⁻¹ belonging to the presence

of adsorbed water in the spectrum of the as-received sample. In the same spectrum, there is a wide region between 3800 and 2800 cm^{-1} that is characteristic of the interaction of the surface with adsorbed water and other molecules. Vacuum treatment at 150 $^{\circ}\text{C}$ leads to the removal of all residuary substances.

Figures S12 and S13 show the IR spectra of the meso- NH_2 -UiO-66 sample after evacuation in the regions of 3800–3400, 3400–2200 and 2200–1000 cm^{-1} , correspondingly. The small intensive band at 3670 cm^{-1} belongs to the stretching vibration of O-H groups in the bridge μ_3 -OH fragments [51]. The band at 3648 cm^{-1} is characteristic of O-H groups in the bridge μ_3 -OH [52] (Figure S12). In the same place, there are two bands of stretching vibration of the $\nu\text{N-H}$ bond at 3497 cm^{-1} (asymmetric) and at 3382 cm^{-1} (symmetric) in the prime amine groups [53–59].

The bands at 3058, 2978, 2947 and 2881 cm^{-1} (Figure S13) characterize the asymmetrical and symmetrical stretching vibrations in $-\text{CH}_3$ and $-\text{CH}_2$ fragments of organic linkers. There are a few bands in the region of 1900–1670 cm^{-1} belonging to overtones of the deformation vibration $\delta\text{C-H}$ bond (nonlinear and multiple) (Figure S14). In the same place (1650–1550 cm^{-1}), there are the bands of the stretching vibration $\nu\text{C-C}$ in the aromatic rings and bands of the bending vibration $\delta\text{N-H}$ in the prime amine. The bands at 1523 and 1465 cm^{-1} belong to $\nu\text{C=C}$ in the aromatic ring. The bands in the 1300–1000 cm^{-1} region belong to the plain deformation vibration of the aromatic ring.

Acidity of meso-UiO-66 and meso- NH_2 -UiO-66

Figure S15 displays the DRIFT spectra of adsorbed CD_3CN at room temperature on both the meso-UiO-66 and meso- NH_2 -UiO-66 samples.

For the meso-UiO-66 sample, CD_3CN adsorption results in two intensive IR bands at 2310 and 2277 cm^{-1} and a band at 2113 cm^{-1} . For the meso- NH_2 -UiO-66 sample, a low intensive band at 2306 cm^{-1} , a more intensive band at 2265 cm^{-1} and a band at 2113 cm^{-1} were observed. The bands at 2310 and 2306 cm^{-1} belong to $\text{C}\equiv\text{N}$ stretching vibrations in CD_3CN adsorbed on Lewis acid sites (LAS) (coordinated unsaturated Zr^{4+} cations) [60–62]. The blue shift of the $\text{C}\equiv\text{N}$ stretching vibration in the adsorbed CD_3CN molecule on these centers is 57 and 53 cm^{-1} in comparison with the gas phase (2253 cm^{-1}) [63]. The bands $\nu\text{C}\equiv\text{N}$ at 2277 and 2265 cm^{-1} belong to CD_3CN adsorbed at the (BAS) Brønsted acid sites (OH-groups). The blue shifts of $\text{C}\equiv\text{N}$ stretching vibration in the adsorbed CD_3CN molecule on these centers are 24 and 12 cm^{-1} . The band at 2113 cm^{-1} belongs to the deformation vibration C-D bond in the CD_3 -group.

The CD_3CN adsorption on BAS results in a red shift of $\nu\text{O-H}$ bands that gives information about the strength of their acidity. Figures S16 and S17 demonstrate the comparison of spectra before and after CD_3CN adsorption on both samples. The difference in the spectra is given in the same place.

After CD_3CN adsorption on the meso-UiO-66 sample (Figure S16), the intensity of the band at 3671 cm^{-1} decreases. At the same time, the wide and intensive band appears with its maximum at 3393 cm^{-1} . The difference (insertion) gives a shift magnitude of 278 cm^{-1} that points to the presence of mean force BAS on the meso-UiO-66 surface. This conclusion is certified by a $\nu\text{C}\equiv\text{N}$ shift (24 cm^{-1} , see Figure S13 description).

After CD_3CN adsorption on the meso- NH_2 -UiO-66 sample (Figure S17), the intensity of the band at 3670 cm^{-1} decreases. At the same time, the low intensive band appears with its maximum at 3474 cm^{-1} . The difference (insertion) gives a shift magnitude of 196 cm^{-1} that points to the presence of low-force BAS on the meso- NH_2 -UiO-66 surface. This conclusion is certified by a $\nu\text{C}\equiv\text{N}$ shift (12 cm^{-1} , see Figure S13 description).

Figures S18 and S19 show DRIFT- CD_3CN spectra in adsorption–desorption process on the meso-UiO-66 and meso- NH_2 -UiO-66 samples, respectively. It can be seen that the intensity of the bands gradually decreases with increased evacuation temperature and vanishes finally at 100 $^{\circ}\text{C}$.

Thus, the presence of the $-\text{NH}_2$ group results in a decrease in both the amount and the strength of acidity. This result is in good agreement with the one given in ref. [64]. Moreover, the obtained data are perfectly consistent with the results of probing and evaluation of the

Brønsted acid sites by titration of the suspensions of the meso-UiO-66 and meso-NH₂-UiO-66 samples performed according to [65,66]. According to these tests, the pH value of the suspensions of the meso-UiO-66 material is 3.01 and that of its meso-NH₂-UiO-66 analog is 6.7.

2.6. Evaluation of the Thermal Stability of the Synthesized micro-UiO-66 and meso-UiO-66 Materials

Evaluation of the thermal stability of the synthesized micro-UiO-66 and meso-UiO-66 materials was carried out using the TGA method in an air atmosphere (S20). In the temperature region before 50 °C, a remarkable weight gain for both samples is observed. This phenomenon could be explained by air humidity sorption. The weight loss of around 8% for the micro-UiO-66 sample and around 5% for the meso-UiO-66 sample in the region of 50–100 °C corresponding to the removal of the adsorbed water molecules are weakly expressed (when compared with the literature data [67]). Therefore, it could be suggested that there is almost no physisorbed in the samples. In the temperature region before 200–400 °C, there is no plateau. Therefore, the analyzed micro-UiO-66 and meso-UiO-66 materials originally presented a dehydrated form of UiO-66-[Zr₆O₆]bdc₆, due to their prolonged activation by heating under a vacuum.

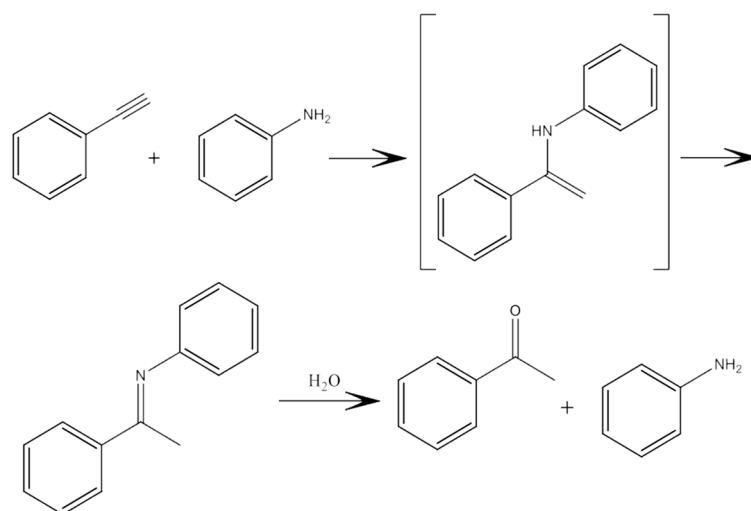
The TGA results reveal that micro-UiO-66 and meso-UiO-66 materials differ in their thermal stability. For the microporous UiO-66 sample, the decomposition temperature is ~310 °C, while for the meso-UiO-66 sample, it is ~440 °C, which is consistent with the literature data [67]. The destruction of both studied samples is finished at 550 °C.

The number of missing linkers per Zr₆O₆ (Table S2) was calculated for the temperature region 310–550 °C according to the literature procedure [67].

2.7. Catalytic Hydroamination of Phenylacetylene with Aniline over Au@meso-UiO-66 and Au@meso-NH₂-UiO-66 Nanohybrids

The synthesized Au@meso-UiO-66 and Au@meso-NH₂-UiO-66 nanohybrids were studied in the hydroamination reaction of phenylacetylene with aniline in an air atmosphere. The pristine meso-UiO-66 material shows very low activity in this process. In particular, the imine yield was around 1% in 3.8 h.

According to A. Corma [68], this regioselective reaction over supported gold nanoparticles occurs via the Markovnikov addition and results in enamine, which then undergoes tautomerization into a more stable imine [phenyl-(1-phenylethylidene)amine] (Scheme 1). This imine is hydrolyzed to acetophenone by traces of water, which may be present in the reaction system. For this reason, the most relevant studies presented in the literature describe carrying out this process in an inert atmosphere.



Scheme 1. Hydroamination of phenylacetylene with aniline over Au-NP.

The reaction conditions, such as reagent ratio and reaction medium were optimized by taking into account the literature data [69]. In particular, it was justified that the optimal PhAc: An ratio should be 1:2. The experimental results show (Table 2, Figure 10 and Figure S21) that carrying out the hydroamination reaction over an Au@meso-NH₂-UiO-66 system without a solvent results in a remarkable gain in activity (expressed in TOF) along with conversion when compared to accomplishing this reaction in the toluene medium.

Table 2. Catalytic performance and recyclability of the Au@meso-UiO-66 and Au@meso-NH₂-UiO-66 nanohybrids in the reaction of hydroamination of phenylacetylene with aniline. Phenylacetylene: aniline molar ratio is 1:2. 1. Au content in the nanocatalysts is ~3.34 wt.% for the Au@meso-UiO-66 and 2.14 wt.% for the Au@meso-NH₂-UiO-66 nanomaterials, respectively.

Catalyst	Cycle	T, h	Conversion, %	Imine Yield, %	Selectivity, %	TOF, h ⁻¹
Meso-UiO-66	1	3.8	1.2	1.0	-	-
Au@meso-UiO-66	1	3.0	75.58	64.80	85.75	65.95
Au@meso-UiO-66	2	3.5	74.04	67.96	91.79	54.00
Au@meso-UiO-66	3	3.8	63.60	52.71	82.88	40.71
Au@meso-UiO-66	1	4.5	92.06	82.57	89.69	63.80
Au@meso-UiO-66	1	6.0	90.90	81.70	89.88	65.95
Au@meso-NH ₂ -UiO-66	1	3.1	62.36	46.83	75.11	128.88
Au@meso-NH ₂ -UiO-66 *	1	3.0	46.99	42.62	90.71	16.57
Au@BIF-66 [42]	1	24.0	74.50	71.00	95.30	22.70
AuNPs-sPSB-t **, *** [16]	1	7.0	90.00			64.00
AuNPs-TiO ₂ *** [16]	1	7.0	90.00			64.00
Au@MCN *** [69]	1	48.0	66.00	65.00	98.00	

Au:PhAc:An = 1:168:336 molar ratio for the Au@meso-UiO-66 system. Au:PhAc:An = 1 molar ratio for the Au@meso-NH₂-UiO-66 system. * Toluene was used as solvent; Au:PhAc:An = 1:29.5:59 molar ratio. ** sPSB—crystalline syndiotactic polystyrene-cis-1,4-polybutadiene multiblock copolymer matrix, which is permeable for reactants; Au:PhAc:An = 1:500:600 molar ratio. ***—The hydroamination reaction was carried out in N₂ atmosphere. MCN—N-doped mesoporous carbon.

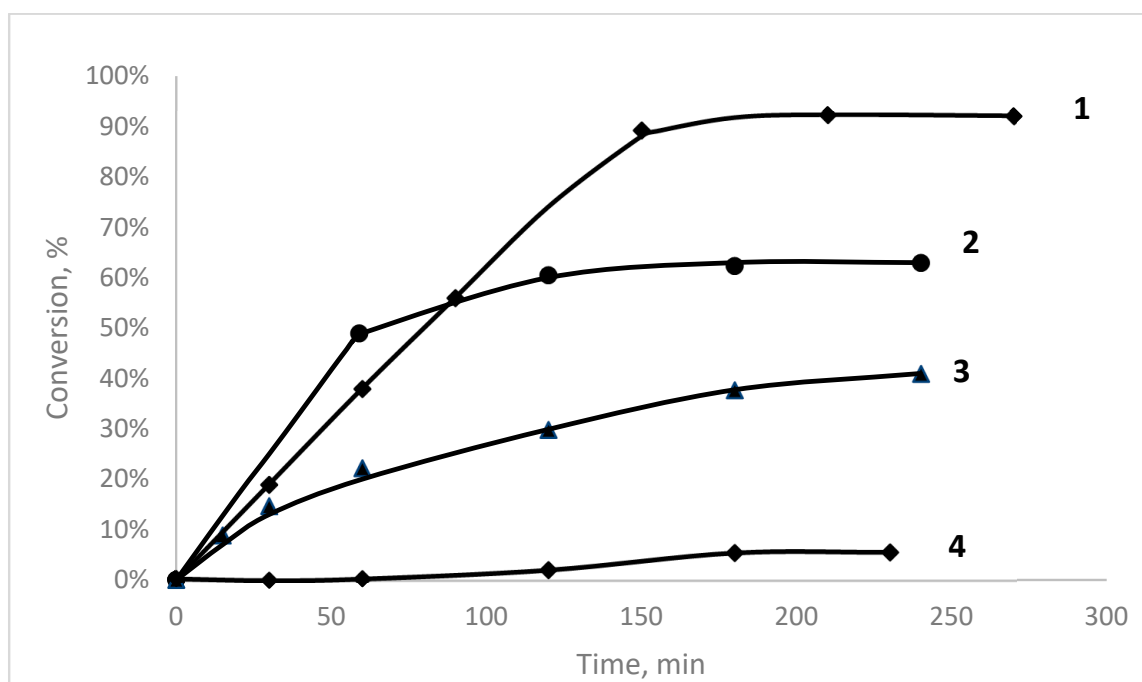


Figure 10. Hydroamination of phenylacetylene with aniline over synthesized nanocatalysts. Phenylacetylene: aniline molar ratio is 1:2. 1. Au@meso-UiO-66 nanocatalyst; without solvent. 2. Au@meso-NH₂-UiO-66 nanocatalyst; without solvent. 3. Au@meso-NH₂-UiO-66 nanocatalyst; toluene used as solvent. 4. Meso-UiO-66 nanocatalyst; without solvent.

In the optimized conditions, the Au@meso-UiO-66 and Au@meso-NH₂-UiO-66 nanohybrids show high activity in the intermolecular hydroamination of phenylacetylene with aniline (Table 2). Using them, the reaction time for the hydroamination is 3–5 h (Table 2, Figure 11). In this period, phenylacetylene conversion values are achieved as high as ~62–91% and imine yields of ~47–83% (Table 2) depending on the catalytic system. These results are comparable or enhanced, as shown by the reported gold-containing catalysts embedded in the polymer [16], inorganic [16], carbon [69] and MOF [42] matrices (Table 2).

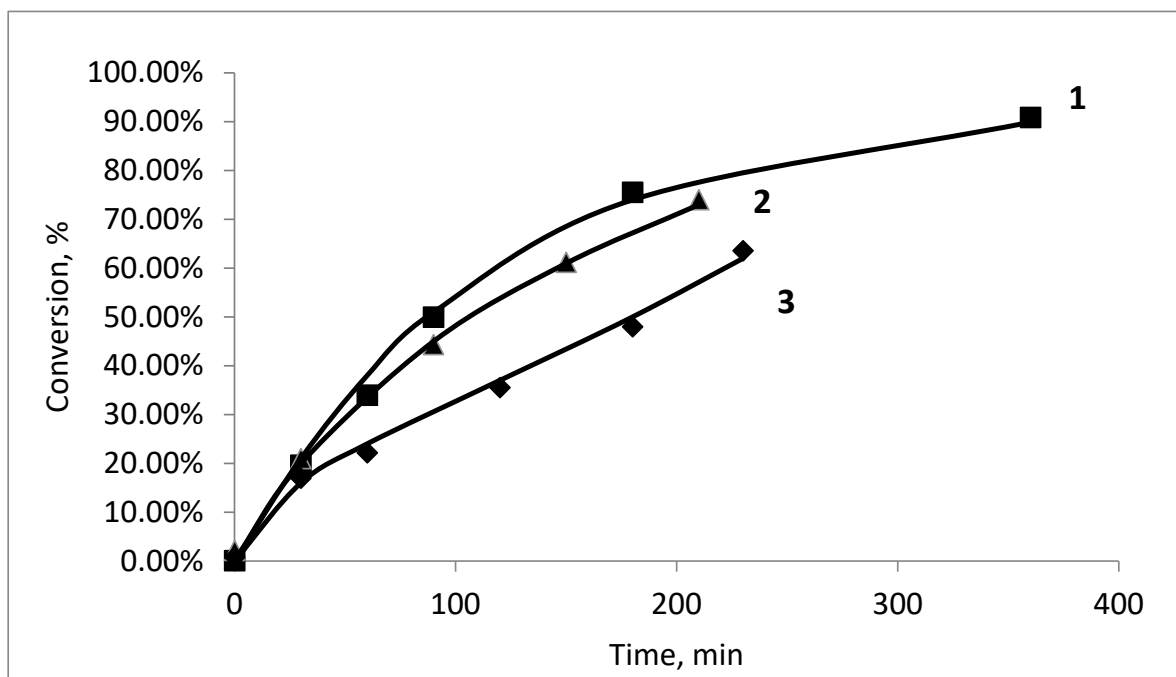


Figure 11. Hydroamination of phenylacetylene with aniline over Au@meso-UiO-66 without solvent. Phenylacetylene: aniline molar ratio is 1:2. 1. 1st cycle; 2. 2nd cycle; 3. 3rd cycle.

Additionally, in the most relevant literature works [16,69], the hydroamination reaction is carried out in a protective inert atmosphere and (often) using molecular sieves in order to exclude water presence in the reaction system and thereby achieve a high selectivity on imine. In this work, the hydroamination of phenylacetylene with aniline is carried out in an air atmosphere without special protection conditions.

The Au@meso-NH₂-UiO-66 nanocatalyst shows an activity expressed in TOF, which is almost twice as high (Figure 10, Table 2) when compared with an activity demonstrated by the Au@meso-UiO-66 counterpart.

Vice versa, the latter system demonstrates a better conversion and target product (imine) yield when compared with Au@meso-NH₂-UiO-66 nanomaterial.

The synthesized gold-containing nanocatalysts show a good selectivity towards imine in the hydroamination reaction. In particular, a high selectivity of around 82–92% achieved at the end of the reaction using the Au@meso-UiO-66 nanohybrid is comparable with the selectivity values reported for gold-containing catalysts based on different supports (Table 2).

Its amino-modified analog, Au@meso-NH₂-UiO-66, exhibits a slightly reduced selectivity (about ~5%). However, by performing hydroamination in the toluene medium, its selectivity improves and reaches around 91%, which is almost equal to the selectivity afforded by the Au@meso-UiO-66 nanocatalyst. Probably, this phenomenon could be explained by the hydrophobicity of toluene, which prevents imine hydrolysis.

The Au@meso-UiO-66 nanohybrid shows high catalytic stability in this reaction. Noteworthy, unlike the Au-containing catalytic systems known from the literature [69], no

special catalyst rinsing and activation before the next catalytic cycle was carried out in the recycling tests.

The activity of the Au@meso-UiO-66 nanohybrid along with the conversion values decreased gradually in three consecutive catalytic cycles (Table 2, Figure 11). In particular, the TOF value decreased slightly (around 8%) in the second catalytic cycle. This activity drop correlates well with the percentage of gold leaching (around 9% of the initial value) after the first catalysis cycle (Table S1). A further decrease in the TOF value was observed in the third catalytic cycle.

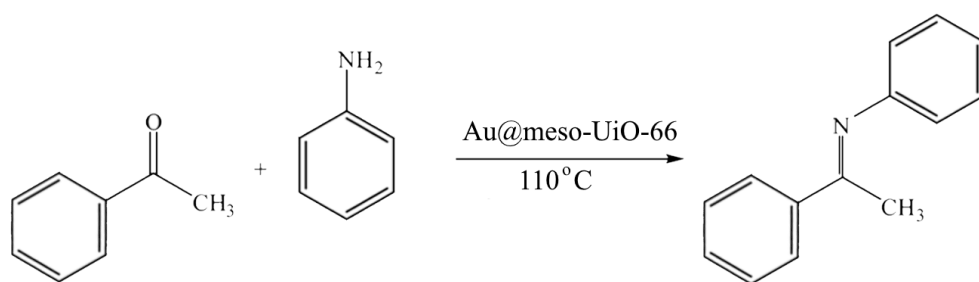
The imine yield remained intact or even increased slightly in the second catalytic cycle. However, its drop of almost 20% was observed in the third catalytic cycle.

As to the process selectivity towards imine, it increased slightly up to 92% in the second cycle and then decreased almost to the level achieved in the first cycle.

Some discrepancies between trends of TOF values, conversions and imine yields in three consecutive catalytic cycles could be assigned to the adsorption–desorption (as a side-process) of reactants and reaction products on the surface of the Au@meso-UiO-66 nanohybrid.

It was mentioned in Section 2.4 that its structural characteristics do not change after three catalytic cycles. However, some gold leaching could be suspected by comparing the XRD patterns for the Au@meso-UiO-66-before-catalysis and the Au@meso-UiO-66-after-catalysis (after three catalytic cycles) nanohybrids. Probably, Au-NP leaching along with a partial blockage of the carrier pores results in the slight catalyst activity drop in the third cycle.

Some impact on the imine yield could also have the reverse reaction of the condensation of aniline, which presents in excess in the reaction system, and acetophenone formed in few quantities (Scheme 2) over studied nanohybrids, which results in the formation of imine. This process could facilitate the target imine yield by involving the condensation of acetophenone (as a by-product). We tested the possibility of this reaction using the Au@meso-UiO-66 nanocatalyst, which showed high activity in this process. The results of this test are presented in Table 3 and Figure 12. They reveal that this nanohybrid shows a high activity in this condensation affording target imine. However, in this case, the TOF value was decreased about four times when compared with the direct hydroamination of phenylacetylene with aniline.



Scheme 2. The condensation reaction of acetophenone and aniline.

Table 3. Catalytic performance and recyclability of the Au@meso-UiO-66 nanohybrid in the reaction of condensation of acetophenone and aniline.

T, h	Conversion, %	Imine Yield, %	TOF, h ⁻¹
3.5	55.42	51.16	11.52

Furthermore, the condensation of acetophenone and aniline could impact the imine yield increase in the second catalytic cycle over the Au@meso-UiO-66 nanohybrid without a remarkable change in conversion values.

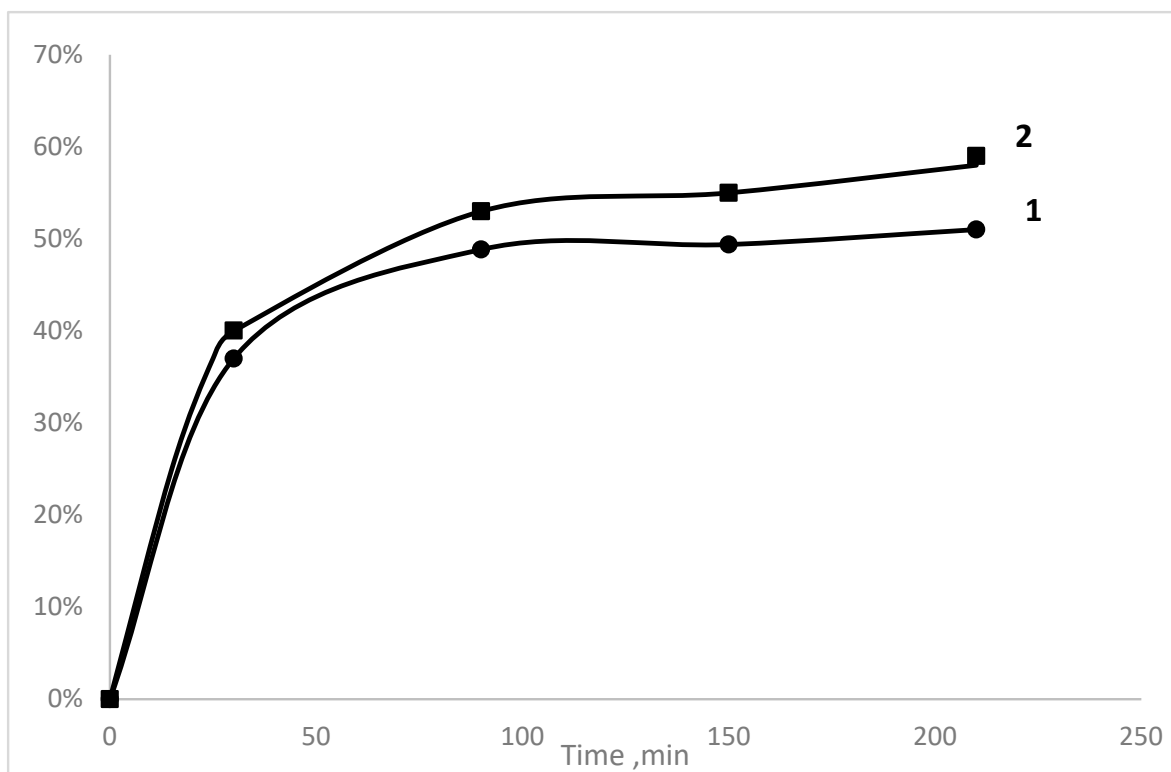


Figure 12. Condensation of acetophenone and aniline over Au@meso-UiO-66 nanocatalyst into imine. Acetophenone:aniline molar ratio is 1:2. 1. Yield; 2. Conversion.

3. Discussion

The obtained results show that using Au-containing hierarchically structured meso-UiO-66 and meso-NH₂-UiO-66 nanomaterials, a high phenylacetylene conversion and imine yield are achieved (Table 2).

It is suggested that the enhanced catalytic performances of the Au@meso-UiO-66 and Au@meso-NH₂-UiO-66 nanohybrids are based on a combination of a number of factors. The first of them is their extremely small crystallite nanosizes, which are below ~8–14 nm. This high dispersion of the carrier nanoparticles could be assigned to the utilization of the MW-activation of the reaction mass for the synthesis of the meso-UiO-66 and meso-NH₂-UiO-66 host matrices. Actually, the MW technique is a well-recognized method for producing inorganic and hybrid materials [70] including UiO-66-type matrices with a high dispersion of the nanoparticles forming them [43,71,72].

A combination of being hierarchically structured with a prevailing mesopore fraction, highly dispersed with very small nanoparticles of both carriers with sizes of ~8 nm (the meso-UiO-66 carrier) and ~14 nm (the meso-NH₂-UiO-66 nanomaterial) along with intrinsic (NH₂)-UiO-66 functionalities provide for stabilization of small Au-NP with average sizes of 7.3–7.8 nm, which is favorable for a hydroamination reaction according to our preliminary studies. Because both nanohybrids have almost the same Au-NP size (7–8 nm), dispersion and location in the porous meso-UiO-66 and meso-NH₂-UiO-66 matrices, the differences in activities of the Au@meso-NH₂-UiO-66 and Au@meso-NH₂-UiO-66 nanohybrids are determined by intrinsic carrier properties.

The meso-UiO-66 and meso-NH₂-UiO-66 carriers composed of small nanocrystallites with short pores provide an efficient decrease in the inner diffusion limitations for the mass transfer of reactants to the Au-NP active size, as well as products from active sites. The differences in the catalytic performances of the Au-containing nanohybrids could be explained, to some extent, by the lower nanoparticle size of the meso-UiO-66 carrier—~8 nm when compared with that for the meso-NH₂-UiO-66 material—14 nm. It is well-known

that a decrease in the size of the carrier nanoparticles with short pores results in a decrease in inner diffusion limitations for the reactant and reaction products [73].

Further reducing mass transport limitations is achieved due to the utilization of mesostructured meso-UiO-66 and meso-NH₂-UiO-66 carriers with a prevailing mesopore fraction (as a result of defect formations associated with missing linkers in the framework) for the Au-NP deposition. The hindered diffusion of the bulky organic molecules to the narrow UiO-66 micropores (0.7 nm in the case of the “classic” microporous metal–organic framework) results in the lower activity of the corresponding catalytic systems [65,74].

The favorable effect of defects in the metal–organic frameworks and in other porous solids as active phase carriers for the transformation of organic molecules including hydroamination was reported in [40,75]. The micro–mesopore structure may facilitate the mass transport of the bulky reagent molecules, i.e., aniline and phenylacetylene, as well as an imine reaction product in their pores. In its turn, gold embedding in the UiO-66-type porous matrices provokes further mesoporosity formation. In particular, increasing the mesopore fraction in the Au@meso-UiO-66-before-catalysis and Au@meso-NH₂-UiO-66-before-catalysis nanohybrids could be explained by the collapse of the certain fraction of micropores during gold deposition. The template effect of Au-NP, which assists the mesopore formation in a MOF porous host, was observed for the zeolitic imidazolate ZIF-8 [71] and ZIF-67 [42] matrices.

The larger mesopore fraction in the meso-UiO-66 carrier provides more space for Au-NP embedding than in the meso-NH₂-UiO-66 matrix. In this case, the micropore content remains almost intact, while in the meso-NH₂-UiO-66 carrier, the micropore volume decreases by four times. Therefore, the preferential location of Au-NP inside the mesopores of the meso-UiO-66 and meso-NH₂-UiO-66 porous hosts could be concluded.

Probably, the presence of remarkable (more than 50% in terms of mesopore volume, cm³/g) mesopore fraction in the meso-UiO-66 and meso-NH₂-UiO-66 matrices contributes to enhancing the catalytic activity of the corresponding Au@meso-UiO-66 and Au@meso-NH₂-UiO-66 nanohybrids. This favorable pore structure may facilitate the mass transport of the bulky reagent molecules, i.e., aniline and phenylacetylene, as well as an imine reaction product in their pores.

However, a decrease in the mesopore volume in the Au@meso-NH₂-UiO-66-after-catalysis nanohybrid when compared to that of the pristine meso-NH₂-UiO-66 matrix and Au@meso-NH₂-UiO-66-before-catalysis nanomaterial could be explained by the partial pore blockage of the carrier by the bulky reagents and reaction products.

The meso-UiO-66 material, with more mesopore fraction and higher specific surface area, provides more diffusion pathways for reaction reagents and products than that of its amino-modified counterpart. Furthermore, partial blockage by reaction products is almost not observed for the Au@meso-UiO-66-after-catalysis nanomaterial after the first catalytic cycle (Table 1). Only after the third cycle could this phenomenon take place, which provokes some activity decrease for this nanocatalyst.

Therefore, the enhanced catalytic performance of the Au@meso-UiO-66-before-catalysis nanohybrid in terms of conversion and imine yield could be explained by the presence of the more significant mesopore volume in the meso-UiO-66 porous matrix.

Furthermore, the formation of mesopores in the UiO-66-type matrices provokes the formation of Brønsted acid sites (as defects or mono-coordinated hbdc linkers) along with μ₃-OH, Zr-OH₂, and Zr-OH sites in a combination with Lewis acid sites as Zr⁴⁺ ions in these frameworks [65]. The Lewis and Brønsted acid sites with different strengths in the meso-UiO-66 and meso-NH₂-UiO-66 matrices may also contribute to the differences in the catalytic activities of the Au@meso-UiO-66 and Au@meso-NH₂-UiO-66 nanohybrids. Additionally, the NH₂-UiO-66 matrix has Brønsted base sites located in amino groups.

Note that the strengths of the Lewis and Brønsted acid sites in the UiO-66 and NH₂-UiO-66 materials provide their activity in a number of catalytic reactions requiring Lewis and/or Brønsted acidity [65], such as the esterification of carboxylic acid [65], citronellal isomerization [65], and the Meerwein-Ponndorf-Verley reduction of cyclohexanone [65].

The Brønsted acidity of the UiO-66-type materials was tested by potentiometric acid-base titration [65]. For each compound, pKa values were determined for the three typical types of protons: μ_3 -OH, Zr-OH₂, and Zr-OH (M = Zr). In the case of the UiO-66 matrix, the pKa values found were 3.52 ± 0.02 , 6.79 ± 0.01 and 8.30 ± 0.02 , respectively.

Lewis and Brønsted acid sites in the meso-UiO-66 carrier may also contribute to the catalytic activity of the Au@meso-UiO-66 and Au@meso-NH₂-UiO-66 nanohybrids. DRIFTS studies and titration of the water suspension of the meso-UiO-66 and meso-NH₂-UiO-66 samples reveal that both carriers differ in their acidity. Probably, the presence of Lewis and Brønsted acid sites with mean strength in the meso-UiO-66 host matrix could assist in the catalytic activity of the Au@meso-UiO-66 nanohybrid based on it. Note that the pristine meso-UiO-66 material could accelerate this transformation to some extent (Table 2).

The meso-NH₂-UiO-66 matrix has weak Lewis and Brønsted acid sites; however, weak Brønsted base sites placed in amino groups impact the catalytic activity of the Au@meso-NH₂-UiO-66 nanocatalyst based on it. The examples of the promoting effect of the bases, including heterogenized metal complexes with amino-containing ligands (amine functionalized environment of the active sites) on the hydroamination reaction of alkynes, are described elsewhere [40,76]. Additionally, the amino-functionality of the meso-NH₂-UiO-66 support may also contribute to the catalyst activity by facilitating the adsorption of the reactants, assisting with their high concentration near the Au-NP active sites. With the reaction progress, the strong adsorption of aniline (which is presented in the reaction mixture in excess) along with the reaction products could block the Au-NP active sites.

The Au@meso-UiO-66 and Au@meso-NH₂-UiO-66 nanomaterials can be regarded as bifunctional catalytic systems. Thanks to a combination of the favorable factors mentioned above, the synthesized Au@meso-UiO-66 and Au@meso-NH₂-UiO-66 nanohybrids demonstrate enhanced catalytic performances when compared with the properties shown by most active gold-containing catalysts deposited on porous supports [16,69] (Table 2).

4. Materials and Methods

All reagents and solvents employed were commercial products (Acros Organics, Antwerpen, Belgium). N,N'-dimethylformamide (DMF) was distilled over CaH₂ under reduced pressure.

4.1. Preparation of meso-UiO-66, meso-NH₂-UiO-66 Host Matrices, and Au@meso-UiO-66 and Au@meso-NH₂-UiO-66 Nanohybrids

Meso-UiO-66 material was synthesized using the MW-assisted method under atmospheric pressure according to original procedure using reagent ratio reported in [32].

ZrOCl₂·8H₂O (1.61 g, 5 mmol) and bdc (0.83 g, 5 mmol) were dissolved separately in two DMF portions (40 mL). The reagent solutions were combined and transferred into a glass ampoule, and then heated in a chamber of an MW oven "Vigor" (200 W, 60 min, 150 °C) at atmospheric pressure. Formed white gel was separated on a centrifuge and washed with DMF (2 × 20 mL), H₂O (2 × 20 mL) and MeOH (2 × 20 mL). The product was dried under reduced pressure and then activated under vacuum (150 °C, 8 h). The yield was 1.271 g (91.7%).

Meso-NH₂-UiO-66 material was synthesized according to original MW-assisted procedure. ZrOCl₂·8H₂O (1.61 g, 5 mmol) and abdc (0.91 g, 5 mmol) were dissolved separately in two DMF portions (40 mL). The reagent solutions were combined and transferred into a glass ampoule and heated at atmospheric pressure in a chamber of an MW oven "Vigor" (200 W, 60 min, 150 °C). The formed pale yellow gel was separated on a centrifuge and washed with DMF (2 × 20 mL), H₂O (2 × 20 mL) and MeOH (2 × 20 mL). The product was dried under reduced pressure and then activated under vacuum (150 °C, 8 h). The yield was 1.341 g (93.1%).

Au@meso-UiO-66 and Au@meso-NH₂-UiO-66 nanohybrids were obtained by stirring the mixture of meso-UiO-66 or meso-NH₂-UiO-66 materials (0.5 g) and HAuCl₄ (24 mg,

58.3 mmol) in MeOH (40 mL) in Ar atmosphere for 5 h. NaBH₄ was added (10 times excess, 22 mg, 0.291 mmol) in MeOH (10 mL) and then stirred for an additional hour at RT before filtration. The fresh catalysts were activated under vacuum at 120 °C for 3 h prior to catalysis.

The gold loading in the Au@meso-UiO-66 and Au@meso-NH₂-UiO-66 nano hybrids was determined by inductively coupled plasma atom emission spectrometry (ICP-AES) with an iCAP 6500 Duo View spectrometer from Thermo Scientific. Prior to ICP-AES analysis, the Au@meso-UiO-66 and Au@meso-NH₂-UiO-66 catalysts (50 mg) were acid-digested with the mixture of nitric and hydrochloric acid in an autoclave.

4.2. Characterization of Synthesized Materials

4.2.1. N₂ Adsorption Data

These data were obtained at 77 K using an ASAP 2020 Plus instrument (Micromeritics, Norcross, GA, USA). The specific surface areas were calculated according to the BET equation (ISO 9277). The total pore volume was evaluated at $p/p_0 = 0.99$. The mesopore volume was calculated as the difference between total pore volume and micropore volume. The distribution in sizes of mesopores was calculated from the desorption branch according to the method of Barrett, Joyner and Halenda (BJH) [77]. The micropore volume was calculated by “t-plot” method. The micropore size distribution was calculated according to the Horwath–Kawazoe model [78] in assumption of a cylinder shape of the pores [79]. Prior to the adsorption measurements, the samples were evacuated (150 °C, 6 h).

4.2.2. Electronic Microscopy Study

Sample microstructure and morphology were studied using a SU8000 field-emission scanning electron microscope (FE-SEM, Hitachi, Mannheim, Germany). The target-oriented approach was utilized for the optimization of the analytical measurements [80]. The samples were mounted on a 3 mm copper grid with a carbon film and fixed in a grid holder. Images were acquired in the bright-field STEM mode at a 30 kV accelerating voltage.

4.2.3. Powder X-ray Diffraction

X-ray powder diffraction data were collected in a reflection mode using an EMPYREAN instrument (PANalytical, Malvern, UK) equipped with a linear X'celerator detector and non-monochromated Cu K α radiation ($\alpha = 1.5418 \text{ \AA}$), measurement parameters: tube voltage/current 40 kV/35 mA, divergence slits of 1/8 and 1/4°, 2 θ range 5–40°, speed 0.2° min⁻¹.

4.2.4. DRIFTS Studies

The Diffuse Reflectance Infrared Fourier Transform Spectra (DRIFTS) were recorded at room temperature with a Nicolet 460 Protégé spectrometer (Woodland, CA, USA) equipped with a diffuse reflectance attachment. The catalysts were placed in an ampoule supplied with a KBr window. Before FTIR spectra collection, the samples were treated in vacuum at 150 °C for 2 h. To obtain a satisfactory signal-to-noise ratio, 500 scans were collected per spectrum. The spectra were measured from 400 to 6000 cm⁻¹ with a resolution of 4 cm⁻¹. The probe molecule for acid sites (CD₃CN) was adsorbed at room temperature and saturated vapor pressures of 96 Torr. The intensity of absorption bands in the spectra was evaluated in Kubelka–Munk units. CaF₂ powder was used as a standard. OMNIC was used for spectra recording and processing.

4.2.5. Evaluation of the Acidity of meso-UiO-66 or meso-NH₂-UiO-66 Materials

The meso-UiO-66 and meso-(NH₂)-UiO-66 samples were dispersed in 50 mL of KCl solution (0.01 M) for 12 h. Then, pH values of suspensions were measured with an ionometer with glassy electrode.

4.2.6. Thermogravimetric Analysis

The dried micro-UiO-66 and meso-UiO-66 samples (~40 mg) were placed in a platinum crucible and heated in air from 20 to 650 °C at a heating rate of 5 °C min⁻¹.

4.3. Catalytic Tests

The catalyst (0.15 g), undecane (as an internal standard for GLC analysis, 0.1 g) were placed in a glass reactor. Then, the reagents, phenylacetylene (0.436 g, 4.27 mmol) and aniline (0.813 g, 8.54 mmol), were added, and the resulting mixture was stirred (110 °C, 3–6 h). The reaction time was selected taking into account the reaction progress. So, the reaction was finished, when the conversion did not change with time. In the catalytic tests involving solvent utilization, the hydroamination reaction was carried out in toluene medium (2 mL).

In the case of hydroamination of acetophenone with aniline, the same reaction conditions were used. The reaction mixture composition was acetophenone (0.513 g, 4.27 mmol) and aniline (0.813 g, 8.54 mmol).

The hydroamination process was monitored by GLC using a Chromatech-Crystal 5000 instrument (Moscow, Russia) with a flame-ionization detector equipped with a capillary column SE-54 (50 m), T = 100–170 °C. Commercially available phenylacetylene, aniline and acetophenone were used as reference samples for the corresponding GLC peaks identification. To identify the imine peak, the reference imine sample synthesized by us previously and identified by ¹H NMR spectroscopy [42] was utilized. In recycling experiments, the catalyst was filtered and re-used without special rinsing.

The catalyst activity was characterized as TOF calculated by Equation (1):

$$\text{TOF} = \frac{n(\text{PhCCH}) \times \eta(\text{PhCCH}, t)}{n(\text{Au}) \times t}, \quad (1)$$

where $n(\text{PhCCH})$ is the initial phenylacetylene loading (mol); $\eta(\text{PhCCH}, t)$ is the phenylacetylene conversion for an initial period of time t (corresponding to the linear section of the conversion curve); $n(\text{Au})$ is the Au loading in the catalyst, mol; t is time, h.

The selectivity to imine was calculated according to the Equation (2):

$$S, \% = \frac{\eta(\text{Imine})}{\eta(\text{Imine}) + \eta(\text{other products}) + \eta(\text{PhAc})} \times 100\% \quad (2)$$

where $\eta(\text{Imine})$ is the imine yield and $\eta(\text{PhAc})$ is the acetophenone yield.

5. Conclusions

In this work, novel Au@meso-UiO-66 and Au@meso-NH₂-UiO-66 nanohybrids were synthesized using hierarchically structured meso-UiO-66 and meso-NH₂-UiO-66 host matrices for Au-NP embedding. The meso-UiO-66 and meso-NH₂-UiO-66 materials were prepared using original procedures realized in the conditions of MW-activation of the reaction mass.

The novel Au@meso-UiO-66 and Au@meso-NH₂-UiO-66 nanohybrids were studied as heterogeneous catalytic systems in the liquid-phase hydroamination of phenylacetylene with aniline under air conditions. The Au@meso-NH₂-UiO-66 nanomaterial demonstrated the best catalytic activity expressed in TOF, while the Au@meso-UiO-66 nanocatalysts showed the highest phenylacetylene conversion and target imine ([phenyl-(1-phenylethylydene)amine]) yield.

Both synthesized Au@meso-UiO-66 and Au@meso-NH₂-UiO-66 nanohybrids showed enhanced catalytic performance in terms of phenylacetylene conversion, target imine yield, activity in TOF and selectivity towards imine when compared to other known heterogeneous systems supported on inorganic and carbon carriers. These excellent catalytic properties could be explained by a number of the cooperative effects arising from an extremely small size of the crystallites constituted by the meso-UiO-66 and NH₂-UiO-66

carriers, their favorable hierarchical micro/mesoporous structure, adsorption ability for the reactants, intrinsic Lewis and Brønsted acid/base sites in these matrices along with a high dispersion of Au-NPs (with sizes of ~7–8 nm) embedded in them.

Supplementary Materials: The following supporting information can be downloaded at: <https://www.mdpi.com/article/10.3390/catal13010133/s1>, Figure S1: Micropore size distribution calculated by the Horwath – Kawazoe method in assumption of a cylinder pore geometry (Saito-Foley). (a)—meso-UiO-66 and Au@meso-UiO-66-before- and -after-catalysis materials); (b)—meso-NH2-UiO-66 and Au@meso-NH2-UiO-66-before- and -after-catalysis materials.; Figure S2: Mesopore size distribution calculated by the BJH method. (a)—meso-UiO-66 and Au@meso-UiO-66-before- and -after-catalysis materials); (b)—meso-NH2-UiO-66 and Au@meso-NH2-UiO-66-before- and -after-catalysis materials); Figure S3: Au-NP distribution on sizes for the Au@meso-UiO-66-before-catalysis nanohybrid; Figure S4: Au-NP distribution on sizes for the Au@meso-NH2-UiO-66-before-catalysis nanohybrid; Figure S5: Au-NP distribution on sizes for the Au@meso-UiO-66-after-catalysis nanohybrid; Figure S6: Au-NP distribution on sizes for the Au@meso-NH2-UiO-66-after-catalysis nanohybrid; Figure S7: DRIFT spectra of both meso-UiO-66 samples before (as received) and after treatment in vacuum at 150 °C in full scale; Figure S8: DRIFT spectrum of meso-UiO-66 sample after evacuation in the region of 3800–3400 cm⁻¹; Figure S9: DRIFT spectrum of meso-UiO-66 sample after evacuation in the region of 3400–2200 cm⁻¹; Figure S10: DRIFT spectrum of meso-UiO-66 sample after evacuation in the region of 2200–1000 cm⁻¹; Figure S11: DRIFT spectra of both meso-NH2-UiO-66 samples before (as received) and after treatment in vacuum at 150 °C in full scale; Figure S12: DRIFT spectrum of meso-NH2-UiO-66 sample after evacuation in the region of 3800–3200 cm⁻¹; Figure S13: DRIFT spectrum of meso-NH2-UiO-66 sample after evacuation in the region of 3200–2200 cm⁻¹; Figure S14: DRIFT spectrum of meso-NH2-UiO-66 sample after evacuation in the region of 2200–1000 cm⁻¹; Figure S15: DRIFT spectra of adsorbed CD3CN at room temperature on meso-UiO-66 and meso-NH2-UiO-66 samples; Figure S16: The comparison of DRIFT spectra before and after CD3CN adsorption on meso-UiO-66 material; Figure S17: The comparison of DRIFT spectra before and after CD3CN adsorption on meso-UiO-66 material; Figure S18: DRIFT-CD3CN spectra in adsorption-desorption process on meso-UiO-66 material; Figure S19: DRIFT-CD3CN spectra in adsorption-desorption process on meso-NH2-UiO-66 sample; Figure S20: TGA curves for the meso-UiO-66 (1) and micro-UiO-66 (2) samples; Figure S21: Hydroamination of phenylacetylene with aniline over Au@meso-NH2-UiO-66 nanohybrid; Toluene used as solvent. The Au wt.% content in the catalyst is 2.14 wt.%; Table S1: Gold content (wt.%) in the Au@meso-UiO-66 and Au@meso-NH2-UiO-66 nanohybrids before and after catalysis; Table S2: The evaluation of the number of missing linkers per hexa-nuclear zirconium node and deficiency extent in the micro-UiO-66 and meso-UiO-66 materials.

Author Contributions: Conceptualization, V.I.I.; methodology, G.S.D., V.V.V., V.V.C. and L.M.G.; software, V.V.C.; validation, D.A.A., G.I.K. and V.V.C.; formal analysis, G.I.K., O.P.T. and V.V.C.; investigation, V.V.V., D.A.A., L.M.G., G.S.D., G.I.K., O.P.T. and V.V.C.; resources, L.M.K. and V.I.I.; data curation, L.M.K. and V.I.I.; writing—original draft preparation, V.I.I.; writing—review and editing, L.M.K. and V.I.I.; visualization, L.M.G., V.V.C. and G.I.K.; supervision, L.M.K. and V.I.I.; project administration, L.M.K. and V.I.I.; funding acquisition, L.M.K. All authors have read and agreed to the published version of the manuscript.

Funding: This research was funded by the Ministry of Science and Higher Education of the Russian Federation, project no. 075-15-2021-591.

Data Availability Statement: The data presented in this study are available on request from the corresponding authors.

Acknowledgments: Electron microscopy characterization was performed in the Department of Structural Studies of Zelinsky Institute of Organic Chemistry, Moscow, Russia.

Conflicts of Interest: The authors declare no conflict of interest.

References

1. Kerru, N.; Gummidi, L.; Maddila, S.; Gangu, K.K.; Jonnalagadda, S.B. A Review on Recent Advances in Nitrogen-Containing Molecules and Their Biological Applications. *Molecules* **2020**, *25*, 1909. [CrossRef] [PubMed]
2. Yin, D.; Li, C.; Ren, H.; Liu, J.; Liang, C. Gold-Palladium-Alloy-Catalyst Loaded UiO-66-NH₂ for Reductive Amination with Nitroarenes Exhibiting High Selectivity. *ChemistrySelect* **2018**, *3*, 5092–5097. [CrossRef]
3. Erken, C.; Hindemith, C.; Weyhermüller, T.; Hölscher, M.; Werlé, C.; Leitner, W. Hydroamination of Aromatic Alkynes to Imines Catalyzed by Pd(II)–Anthraphos Complexes. *ACS Omega* **2020**, *5*, 8912–8918. [CrossRef]
4. Meng, J.; Xiao, Y.; Huang, Y.; Liu, X.; Zhao, J. Solvent-free hydroamination of phenylacetylene by plasmonic gold nanoparticles coupled with a TiO₂ 2D photonic layer on nanotube arrays. *New J. Chem.* **2020**, *44*, 17289–17295. [CrossRef]
5. Severin, R.; Doye, S. The catalytic hydroamination of alkynes. *Chem. Soc. Rev.* **2007**, *36*, 1407–1420. [CrossRef]
6. Jimenez, O.; Mueller, T.E.; Schwieger, W.; Lercher, J.A. Hydroamination Reactions Catalyzed with Beta Zeolite. In *Studies in Surface Science and Catalysis*; Elsevier: Amsterdam, The Netherlands, 2004; Volume 105, Part C, pp. 2788–2794.
7. Beerhues, J.; Walter, R.R.M.; Aberhan, H.; Neubrand, M.; Porré, M.; Sarkar, B. Spotlight on Ligand Effects in 1,2,3-Triazolylidene Gold Complexes for Hydroamination Catalysis: Synthesis and Catalytic Application of an Activated MIC Gold Triflimide Complex and Various MIC Gold Chloride Complexes. *Organometallics* **2021**, *40*, 1077–1085. [CrossRef]
8. Isaeva, V.I.; Kustov, L.M. Catalytic Hydroamination of Unsaturated Hydrocarbons. *Top. Catal.* **2016**, *59*, 1196–1206. [CrossRef]
9. Isaeva, V.I.; Prokudina, N.I.; Kozlova, L.M.; Kustov, L.M.; Glukhov, L.M.; Tarasov, A.L.; Beletskaya, I.P. Hydroamination of Phenylacetylene in the Presence of Gold-containing Catalytic Systems Supported on Carriers Modified by Ionic Liquids. *Russ. Chem. Bull. Int. Ed.* **2015**, *64*, 2811–2815. [CrossRef]
10. Corma, A.; Garcia, H. Supported gold nanoparticles as catalysts for organic reactions. *Chem. Soc. Rev.* **2008**, *37*, 2096–2126. [CrossRef]
11. Lee, L.-C.; Zhao, Y. Room Temperature Hydroamination of Alkynes Catalyzed by Gold Clusters in Interfacially Cross-Linked Reverse Micelles. *ACS Catal.* **2014**, *4*, 688–691. [CrossRef]
12. Zhao, J.; Ge, L.; Yuan, H.; Liu, Y.; Gui, Y.; Zhang, B.; Zhou, L.; Fang, S. Heterogeneous Gold Catalysts for Selective Hydrogenation: From Nanoparticles to Atomically Precise Nanoclusters. *Nanoscale* **2019**, *11*, 11429–11436. [CrossRef] [PubMed]
13. Seral-Ascaso, A.; Luquin, A.; Lázaro, M.J.; de la Fuente, G.F.; Laguna, M.; Muñoz, E. Synthesis and Application of Gold-Carbon Hybrids as Catalysts for the Hydroamination of Alkynes. *Appl. Catal. A* **2013**, *456*, 88–95. [CrossRef]
14. Ventura-Espinosa, D.; Sabater, S.; Mata, J.A. Enhancement of gold catalytic activity and stability by immobilization on the surface of graphene. *J. Catal.* **2017**, *352*, 498–504. [CrossRef]
15. Carabineiro, S.A.C. Supported Gold Nanoparticles as Catalysts for the Oxidation of Alcohols and Alkanes. *Front. Chem.* **2019**, *7*, 702. [CrossRef]
16. Litta, A.D.; Buonerba, A.; Casu, A.; Falqui, A.; Capacchione, C.; Franconetti, A.; Garcia, H.; Grassi, A. Highly efficient hydroamination of phenylacetylenes with anilines catalysed by gold nanoparticles embedded in nanoporous polymer matrix: Insight into the reaction mechanism by kinetic and DFT investigations. *J. Catal.* **2021**, *400*, 71–82. [CrossRef]
17. Tronhauser, T.; Mattson, E.; Cocq, K.; Assi, H.; Jensen, S.; Tan, K.; Catalano, M.; Yuan, S.; Wang, H.; Feng, L.; et al. High Stability of Ultra-small and Isolated Gold Nanoparticles in Metal-Organic Framework Materials. *J. Mater. Chem. A* **2019**, *7*, 17536–17546.
18. Phan, A.; Doonan, C.J.; Uribe-Romo, F.J.; Knobler, C.B.; O’Keeffe, M.; Yaghi, O.M. Synthesis, Structure, and Carbon Dioxide Capture Properties of Zeolitic Imidazolate Frameworks. *Acc. Chem. Res.* **2010**, *43*, 58–67. [CrossRef]
19. Qin, L.; Li, Y.; Liang, F.; Li, L.; Lan, Y.; Li, Z.; Lu, X.; Yang, M.; Ma, D. A microporous 2D cobalt-based MOF with pyridyl sites and open metal sites for selective adsorption of CO₂. *Microporous Mesoporous Mater.* **2022**, *341*, 112098. [CrossRef]
20. Liu, J.; Wang, W.; Luo, Z.; Li, B.; Yuan, D. Microporous Metal–Organic Framework Based on Ligand-Truncation Strategy with High Performance for Gas Adsorption and Separation. *Inorg. Chem.* **2017**, *56*, 10215–10219. [CrossRef]
21. Bavykina, A.; Kolobov, N.; Khan, I.S.; Bau, J.A.; Ramirez, A.; Gascon, J. Metal-Organic Frameworks in Heterogeneous Catalysis: Recent Progress, New Trends, and Future Perspectives. *Chem. Rev.* **2020**, *120*, 8468–8535. [CrossRef]
22. Zhong, G.; Liu, D.; Zhang, J. The application of ZIF-67 and its derivatives: Adsorption, separation, electrochemistry and catalysts. *J. Mater. Chem. A* **2018**, *6*, 1887–1899. [CrossRef]
23. Qin, L.; Liang, F.; Li, Y.; Wu, J.; Guan, S.; Wu, M.; Xie, S.; Luo, M.; Ma, D. A 2D Porous Zinc-Organic Framework Platform for Loading of 5-Fluorouracil. *Inorganics* **2022**, *10*, 202. [CrossRef]
24. Chen, J.; Cheng, F.; Luo, D.; Huang, J.; Ouyang, J.; Nezamzadeh-Ejhi, A.; Khan, M.S.; Liu, J.-Q.; Peng, Y. Recent advances in Ti-based MOFs in biomedical applications. *Dalton Trans.* **2022**, *51*, 14817–14832. [CrossRef] [PubMed]
25. Li, M.; Yin, S.; Lin, M.; Chen, X.; Pan, Y.; Peng, Y.; Sun, J.; Kumar, A.; Liu, J. Current status and prospects of metal–organic frameworks for bone therapy and bone repair. *J. Mater. Chem. B* **2022**, *10*, 5105–5128. [CrossRef]
26. Zheng, R.; Guo, J.; Cai, X.; Bin, L.; Lu, C.; Singh, A.; Trivedi, M.; Kumar, A.; Liu, J. Manganese complexes and manganese-based metal-organic frameworks as contrast agents in MRI and chemotherapeutics agents: Applications and prospects. *Colloids Surf. B Biointerfaces* **2022**, *213*, 112432. [CrossRef] [PubMed]
27. Liu, W.; Yan, Q.; Xia, C.; Wang, X.; Kumar, A.; Wang, Y.; Liu, Y.; Pan, Y.; Liu, J. Recent advances in cell membrane coated metal–organic frameworks (MOFs) for tumor therapy. *J. Mater. Chem. B* **2021**, *9*, 4459–4474. [CrossRef] [PubMed]
28. Ji, Z.; Wang, H.; Canossa, S.; Wuttke, S.; Yaghi, O.M. Pore Chemistry of Metal–Organic Frameworks. *Adv. Funct. Mater.* **2020**, *30*, 2000238. [CrossRef]

29. Jiao, L.; Seo, J.Y.R.; Skinner, W.S.; Wang, Z.U.; Jiang, H.-L. Metal-organic frameworks: Structures and functional applications. *Mater. Today* **2019**, *27*, 43–68. [[CrossRef](#)]
30. Yu, J.; Mu, C.; Yan, B.; Qin, X.; Shen, C.; Xue, H.; Pang, H. Nanoparticle/MOF composites: Preparations and applications. *Mater. Horiz.* **2017**, *4*, 557–569. [[CrossRef](#)]
31. Chughtai, A.H.; Ahmad, N.; Younus, H.A.; Laypkov, A.; Verpoort, F. Metal-organic frameworks: Versatile heterogeneous catalysts for efficient catalytic organic transformations. *Chem. Soc. Rev.* **2015**, *44*, 6804–6849. [[CrossRef](#)]
32. Cavka, J.H.; Jakobsen, S.; Olsbye, U.; Guillou, N.; Lamberti, C.; Bordiga, S.; Lillerud, K.P. A New Zirconium Inorganic Building Brick Forming Metal Organic Frameworks with Exceptional Stability. *J. Am. Chem. Soc.* **2008**, *130*, 13850–13851. [[CrossRef](#)] [[PubMed](#)]
33. Isaeva, V.I.; Nefedov, O.M.; Kustov, L.M. Metal-Organic Frameworks-Based Catalysts for Biomass Processing. *Catalysts* **2018**, *8*, 368. [[CrossRef](#)]
34. Caratelli, C.; Hajek, J.; Cirujano, F.G.; Waroquier, M.; Llabrés i Xamena, F.X.; Van Speybroeck, V. Nature of active sites on UiO-66 and beneficial influence of water in the catalysis of Fischer esterification. *J. Catal.* **2017**, *352*, 401–414. [[CrossRef](#)]
35. Vermoortele, F.; Vandichel, M.; Van de Voorde, B.; Ameloot, R.; Waroquier, M.; Van Speybroeck, V.; De Vos, D.E. Electronic Effects of Linker Substitution on Lewis Acid Catalysis with Metal-Organic Frameworks. *Angew. Chem. Int. Ed.* **2012**, *51*, 4887–4890. [[CrossRef](#)]
36. Herbst, A.; Janiak, C. MOF catalysts in biomass upgrading towards value-added fine chemicals. *CrystEngComm.* **2017**, *19*, 4092–4117. [[CrossRef](#)]
37. Shearer, G.C.; Chavan, S.; Ethiraj, J.; Vitillo, J.G.; Svelle, S.; Olsbye, U.; Lamberti, C.; Bordiga, S.; Lillerud, K.P. Tuned to perfection: Ironing out the defects in metal-organic framework UiO-66. *Chem. Mater.* **2014**, *26*, 4068–4071. [[CrossRef](#)]
38. Leus, K.; Concepcion, P.; Vandichel, M.; Meledina, M.; Gorrane, A.; Esquivel, D.; Turner, S.; Poelman, D.; Waroquier, M.; Van Speybroeck, V.; et al. Au@UiO-66: A base free oxidation catalyst. *RSC Adv.* **2015**, *5*, 22334–22342. [[CrossRef](#)]
39. Hinde, C.S.; Webb, W.R.; Chew, B.K.J.; Tan, H.R.; Zhang, W.-H.; Hor, T.S.A.; Raja, R. Utilisation of gold nanoparticles on amine-functionalised UiO-66 (NH₂-UiO-66) nanocrystals for selective tandem catalytic reactions. *Chem. Commun.* **2016**, *52*, 6557–6560. [[CrossRef](#)]
40. Cirujano, F.G.; Lopez-Maya, E.; Navarro, J.A.R.; De Vos, D.E. Pd(II)-Ni(II) Pyrazolate Framework as Active and Recyclable Catalyst for the Hydroamination of Terminal Alkynes. *Top. Catal.* **2018**, *61*, 1414–1423. [[CrossRef](#)]
41. Isaeva, V.I.; Kustov, L.M.; Kapustin, G.I.; Deiko, G.S.; Belyaeva, E.V.; Zizganova, A.I.; Tkachenko, O.P. Gold-Containing Catalysts Based on Mesoporous Metal-Organic Frameworks of the MIL Type for Regioselective Hydroamination Reaction of Phenylacetylene. *Petrol. Chem.* **2020**, *60*, 895–902. [[CrossRef](#)]
42. Isaeva, V.I.; Papathanasiou, K.; Chernyshev, V.V.; Glukhov, L.; Deyko, G.; Bisht, K.K.; Tkachenko, O.P.; Savilov, S.V.; Davshan, N.A.; Kustov, L.M. Hydroamination of Phenylacetylene with Aniline over Gold Nanoparticles Embedded in the Boron Imidazolate Framework BIF-66 and Zeolitic Imidazolate Framework ZIF-67. *ACS Appl. Mater. Interfaces* **2021**, *13*, 59803–59819. [[CrossRef](#)] [[PubMed](#)]
43. Ge, J.; Liu, L.; Shen, Y. Facile synthesis of amine-functionalized UiO-66 by microwave method and application for methylene blue adsorption. *J. Porous Mater.* **2017**, *24*, 647–655. [[CrossRef](#)]
44. Jura, G.; Harkins, W.D. Surfaces of Solids. XI. Determination of the Decrease (π) of Free Surface Energy of a Solid by an Adsorbed Film. *J. Am. Chem. Soc.* **1944**, *66*, 1356–1362. [[CrossRef](#)]
45. Esken, D.; Turner, S.; Lebedev, O.I.; Van Tendeloo, G.; Fischer, R.A. Au@ZIFs—Stabilization and Encapsulation of Cavity-Size Matching Gold Clusters inside Functionalized Zeolite Imidazolate Frameworks, ZIFs. *Chem. Mater.* **2010**, *22*, 6393–6401. [[CrossRef](#)]
46. Zlokazov, V.B.; Chernyshev, V.V. MRSA- a program for a full profile analysis of powder multiphase neutron-diffraction time-of-flight (direct and Fourier) spectra. *J. Appl. Crystallogr.* **1992**, *25*, 447–451. [[CrossRef](#)]
47. Stakheev, A.Y.; Isaeva, V.I.; Markov, P.V.; Turova, O.V.; Mashkovskii, I.S.; Kapustin, G.I.; Saifutdinov, B.R.; Kustov, L. Novel catalysts for selective hydrogenation of C≡C bond based on Pd nanoparticles immobilized in phenylencarboxylate frameworks (NH₂)-MIL-53(Al). *Russ. Chem. Bull. Int. Ed.* **2015**, *64*, 284–290. [[CrossRef](#)]
48. Köck, E.-M.; Kogler, M.; Götsch, T.; Schlicker, L.; Bekheet, M.F.; Doran, A.; Gurlo, A.; Klötzer, B.; Petermüller, B.; Schildhammer, D.; et al. Surface chemistry of pure tetragonal ZrO₂ and gas-phase dependence of the tetragonal-to-monoclinic ZrO₂ transformation. *Dalton Trans.* **2017**, *46*, 4554–4570. [[CrossRef](#)]
49. Jung, K.-D.; Bell, A.T. Role of Hydrogen Spillover in Methanol Synthesis over Cu/ZrO₂. *J. Catal.* **2000**, *193*, 207–223. [[CrossRef](#)]
50. Ouyang, F.; Kondo, J.N.; Maruya, K.-C.; Domen, K. Isotope-exchange reaction between hydrogen molecules and surface hydroxy groups on bare and modified ZrO₂. *J. Chem. Soc. Faraday Trans.* **1996**, *92*, 4491–4495. [[CrossRef](#)]
51. Tsyganenko, A.; Filimonov, V. Infrared spectra of surface hydroxyl groups and crystalline structure of oxides. *J. Mol. Struct.* **1973**, *19*, 579–589. [[CrossRef](#)]
52. Ivanov, A.V.; Kustov, L. Properties of surface acid sites of ZrO₂ and SO₄ZrO₂-based systems studied by diffuse-reflectance Fourier-transform IR spectroscopy: Adsorption of acetonitrile-d₃. *Russ. Chem. Bull.* **2000**, *49*, 39–45. [[CrossRef](#)]
53. Cheng, X.; Zhang, A.; Hou, K.; Liu, M.; Wang, Y.; Song, C.; Zhang, G.; Guo, X. Size- and morphology-controlled NH₂-MIL-53(Al) prepared in DMF–water mixed solvents. *Dalton Trans.* **2013**, *42*, 13698–13705. [[CrossRef](#)]

54. Zhang, S.; Zhou, L.; Chen, M. Amine-functionalized MIL-53(Al) with embedded ruthenium nanoparticles as a highly efficient catalyst for the hydrolytic dehydrogenation of ammonia borane. *RSC Adv.* **2018**, *8*, 12282–12291. [[CrossRef](#)] [[PubMed](#)]
55. Abedini, R.; Omidkhah, M.; Dorosti, F. Highly permeable poly (4-methyl-1-pentyne)/NH₂-MIL 53 (Al) mixed matrix membrane for CO₂/CH₄ separation. *RSC Adv.* **2014**, *4*, 36522–36537. [[CrossRef](#)]
56. Guan, Y.; Xia, M.; Wang, X.; Cao, W.; Marchetti, A. Water-based preparation of nano-sized NH₂-MIL-53(Al) frameworks for enhanced dye removal. *Inorg. Chim. Acta* **2018**, *484*, 180–184. [[CrossRef](#)]
57. Marx, S.; Kleist, W.; Huang, J.; Maciejewski, M.; Baiker, A. Tuning functional sites and thermal stability of mixed-linker MOFs based on MIL-53(Al). *Dalton Trans.* **2010**, *39*, 3795–3798. [[CrossRef](#)]
58. Wang, Y.; Xie, J.; Wu, Y.; Hu, X. A magnetic metal-organic framework as a new sorbent for solid-phase extraction of copper(II), and its determination by electrothermal AAS. *Microchim. Acta* **2014**, *181*, 949–956. [[CrossRef](#)]
59. Isaeva, V.I.; Vedenyapina, M.D.; Kulaishin, S.A.; Lobova, A.A.; Chernyshev, V.V.; Kapustin, G.I.; Tkachenko, O.P.; Ergun, V.V.; Arkhipov, D.A.; Nissenbaum, V.D.; et al. Adsorption of 2,4-dichlorophenoxyacetic acid in an aqueous medium on nanoscale MIL-53(Al) type materials. *Dalton Trans.* **2019**, *48*, 15091–15104. [[CrossRef](#)]
60. Medin, A.S.; Borovkov, V.Y.; Kazansky, V.B.; Pelmentschikov, A.G.; Zhidomirov, G.M. On the unusual mechanism of Lewis acidity manifestation in HZSM-5 zeolites. *Zeolites* **1990**, *10*, 668–673. [[CrossRef](#)]
61. Haney, M.A.; Franklin, J.L. Mass spectrometric determination of the proton affinities of various molecules. *J. Phys. Chem.* **1969**, *73*, 4328–4331. [[CrossRef](#)]
62. Angell, C.L.; Howell, M.V. FTIR Spectroscopic Study of Titanium-Containing Mesoporous Silicate Materials. *J. Phys. Chem.* **1969**, *73*, 2551. [[CrossRef](#)]
63. Purcell, K.F.; Drago, R.S. Studies of the Bonding in Acetonitrile Adducts. *J. Am. Chem. Soc.* **1966**, *88*, 919–924. [[CrossRef](#)]
64. Chakarova, K.; Strauss, I.; Mihaylov, M.; Drenchev, N.; Hadjiivanov, K. Evolution of acid and basic sites in UiO-66 and UiO-66-NH₂ metal-organic frameworks: FTIR study by probe molecules. *Mesopor. Micropor. Mater.* **2019**, *281*, 110–122. [[CrossRef](#)]
65. Cirujano, F.G.; Llabrés i Xamena, F.X.L. Tuning the Catalytic Properties of UiO-66 Metal–Organic Frameworks: From Lewis to Defect-Induced Brønsted Acidity. *J. Phys. Chem. Lett.* **2020**, *11*, 4879–4890. [[CrossRef](#)]
66. Klet, R.C.; Liu, Y.; Wang, T.C.; Hupp, J.T.; Farha, O.K. Evaluation of Brønsted acidity and proton topology in Zr- and Hf-based metal–organic frameworks using potentiometric acid–base titration. *J. Mater. Chem. A* **2016**, *4*, 1479–1485. [[CrossRef](#)]
67. Athar, M.; Rzepka, P.; Thoeny, D.; Ranocchiari, M.; van Bokhoven, J.A. Thermal degradation of defective high-surface-area UiO-66 in different gaseous environments. *RSC Adv.* **2021**, *11*, 38849–38855. [[CrossRef](#)] [[PubMed](#)]
68. Corma, A.; Concepción, P.; Domínguez, I.; Forné, V.; Sabater, M.J. Gold Supported on a Biopolymer (Chitosan) Catalyzes the Regioselective Hydroamination of Alkynes. *J. Catal.* **2007**, *251*, 39–47. [[CrossRef](#)]
69. Sengupta, M.; Bag, A.; Das, S.; Shukla, A.; Konathala, L.N.S.; Naidu, C.A.; Bordoloi, A. Reaction and Mechanistic Studies of Heterogeneous Hydroamination over Support-Stabilized Gold Nanoparticles. *ChemCatChem* **2016**, *8*, 3121–3130. [[CrossRef](#)]
70. Isaeva, V.I.; Tarasov, A.L.; Chernyshev, V.V.; Kustov, L.M. Control of morphology and size of microporous framework MIL-53(Al) crystals by synthesis procedure. *Mendeleev Commun.* **2015**, *25*, 466–467. [[CrossRef](#)]
71. Li, S.; Zhang, W.; Huo, F. The structural and catalytic properties of nanoparticles@MOF composites: A case study of Au@ZIF-8 hybrid crystals. *Phys. E Low-Dimens. Syst. Nanostruct.* **2015**, *69*, 56–60. [[CrossRef](#)]
72. Luan, Y.; Qi, Y.; Gao, H.; Zheng, N.; Wang, G. Synthesis of an amino-functionalized metal–organic framework at a nanoscale level for gold nanoparticle deposition and catalysis. *J. Mater. Chem. A* **2014**, *2*, 20588–20596. [[CrossRef](#)]
73. Isaeva, V.I.; Eliseev, O.L.; Kazantsev, R.V.; Chernyshev, V.V.; Tarasov, A.L.; Davydov, P.E.; Lapidus, A.L.; Kustov, L.M. Effect of the support morphology on the performance of Co nanoparticles deposited on metal–organic framework MIL-53(Al) in Fischer–Tropsch synthesis. *Polyhedron* **2019**, *157*, 389–395. [[CrossRef](#)]
74. Martín, N.; Cirujano, F.G. Organic synthesis of high added value molecules with MOF catalysts. *Org. Biomol. Chem.* **2020**, *18*, 8058–8073. [[CrossRef](#)]
75. Cirujano, F.G.; Dhakshinamoorthy, A. Supported metals on porous solids as heterogeneous catalysts for the synthesis of propargylamines. *New J. Chem.* **2022**, *46*, 1469–1482. [[CrossRef](#)]
76. Patel, M.; Saunthwal, R.K.; Verma, A.K. Base-Mediated Hydroamination of Alkynes. *Acc. Chem. Res.* **2017**, *50*, 240–254. [[CrossRef](#)]
77. Barrett, E.P.; Joyner, L.G.; Halenda, P.P. The determination of pore volume and area distributions in porous substances. I. Computations from nitrogen isotherms. *J. Am. Chem. Soc.* **1951**, *73*, 373. [[CrossRef](#)]
78. Horvath, G.; Kawazoe, K. Method for the calculation of effective pore size distribution in molecular sieve carbon. *J. Chem. Eng. Jpn.* **1983**, *16*, 470–475. [[CrossRef](#)]
79. Saito, A.; Foley, H.C. Curvature and parametric sensitivity in models for adsorption in micropores. *AIChE J.* **1991**, *37*, 429. [[CrossRef](#)]
80. Kashin, A.S.; Ananikov, V.P. A SEM study of nanosized metal films and metal nanoparticles obtained by magnetron sputtering. *Russ. Chem. Bull.* **2011**, *60*, 2602–2607. [[CrossRef](#)]

Disclaimer/Publisher’s Note: The statements, opinions and data contained in all publications are solely those of the individual author(s) and contributor(s) and not of MDPI and/or the editor(s). MDPI and/or the editor(s) disclaim responsibility for any injury to people or property resulting from any ideas, methods, instructions or products referred to in the content.